Impact of roughness length on WRF simulated Land-Atmosphere interactions over a hyper-arid region

Narendra Reddy Nelli[1], Marouane Temimi[1]*, Ricardo Morais Fonseca[1], Michael John Weston[1], Mohana Satyanarayana Thota[1,2], Vineeth Krishnan Valappil[1], Oliver Branch[3], Volker Wulfmeyer[3], Youssef Wehbe[1,4], Taha Al Hosary[4], Abdeltawab Shalaby[4], Noor Al Shamsi[4], Hajer Al Naqbi[4]

[1]Khalifa University of Science and Technology, P.O. Box 54224, Abu Dhabi, United Arab Emirates

[2]National Center for Medium Range Weather Forecasting, Noida-201309, India

[3]Institute of Physics and Meteorology, University of Hohenheim, Germany

[4]National Center of Meteorology, Abu Dhabi, United Arab Emirates

*Correspondence: marouane.temimi@ku.ac.ae, Tel.: +971 2 810 9116

Key Points

1) For the first time, aerodynamic roughness length is estimated from in the United Arab Emirates and it is one order smaller than the default value used in WRF
2) WRF model 2-m air temperature and sensible heat simulations are more accurate with the updated roughness length
3) For wind speeds > 6 m s^{-1}, the model underestimates the strength of the surface wind and it is corrected by 1-3 m s^{-1}, when the updated roughness length is considered

Abstract

The aerodynamic roughness length is a crucial parameter that controls surface variables including the horizontal wind, surface temperature, and heat fluxes. Despite its importance, in the Weather Research and Forecasting (WRF) model, this parameter is typically assigned a predefined value, mostly based on the dominant land-use type. In this work, the roughness length is first estimated from eddy-covariance measurements at Al Ain in the United Arab Emirates (UAE), a hyper-arid region, and then ingested into WRF. The estimated roughness length is in the range 1.3 to 2.2 mm, one order smaller than the default value used in WRF.

In line with previous studies, and from WRF model simulations during the warm and cold seasons, it is concluded that, when the roughness length is decreased by an order of magnitude, the horizontal wind speed increases by up to 1 m s^{-1}, the surface temperature rises by up to 2.5ºC, and the sensible heat flux decreases by as much as 10 W m^{-2}. In comparison with in situ station and eddy covariance data, and when forced with the updated roughness length, WRF gives more accurate 2-m air temperature and sensible heat flux predictions. For prevailing wind speeds > 6 m s^{-1}, the model underestimates the strength of the near-surface wind, a tendency that can be partially corrected, typically by 1-3 m s^{-1}, when the updated roughness length is considered. For low wind speeds (< 4 m s^{-1}), however, WRF generally overestimates the strength of the wind.

Keywords:
Aerodynamic roughness length, near-surface wind speed, sensible heat flux, surface temperature, WRF model, hyper-arid region

1. Introduction

The aerodynamic (or momentum) roughness length (z_{0m}) is the height at which the logarithmic extrapolation of the horizontal wind speed in the surface layer assumes the zero value. It is physically related to the geometric roughness of the underlying elements for aerodynamically rough surfaces, being roughly $1/10^{th}$ of the height of the roughness elements [e.g. *Wallace and Hobbs*, 2006]. A realistic representation of the roughness length is essential for an accurate estimation of the surface transport of momentum, heat and moisture, based on the Monin–Obukhov (M–O) theory and the similarity relations of *Dyer and Hicks* [1970] and *Businger et al.* [1971], an approach widely used in weather and climate models [e.g. *Miller et al.*, 1992; *Dudhia and Bresch*, 2002]. To employ realistic roughness lengths in numerical models is rather challenging, as they are generally a function of the heterogeneity of the land-surface [*Reddy and Rao*, 2016]. The surface roughness of a site is one of the most important parameters which determines the wind flow. In particular, a rough surface retards the flow compared to a smooth surface, which results in a sharp decrease of the near-surface wind speed, and subsequently in changes in the vertical atmospheric profiles and stability [*Rao*, 1996].

Numerical model simulations are known to be very sensitive to land-surface parameters such as vegetation [e.g. *Shukla and Mintz*, 1982; *Hong et al.*, 2009; *Rao et al.*, 2011], soil moisture and thermal conductivity [e.g. *Massey et al.*, 2014], and surface roughness length [e.g. *Sud and Smith*, 1985; *Meehl and Washington*, 1988]. *Sud and Smith* [1985] found that, when the surface roughness length is reduced from 45 to 0.02 cm, the rainfall over the Sahara desert is greatly decreased by roughly 4 mm day^{-1}. *Reijmer et al.* [2004] concluded that a change in the roughness length over Antarctica by about three orders of magnitude gives monthly averaged wind speed, air temperature and sensible heat flux differences of ±2 m s^{-1}, ±10 K and ±35 W m^{-2},

71 respectively. For a vegetated site in the Netherlands, *Giorgi* [1997] noted that an increase in the
72 roughness length from 0.15 to 0.4 m led to a drop in surface temperature and a rise in sensible
73 heat flux by roughly 0.4 ^{o}C and 4 W m^{-2}, respectively. For a further increment in $z_{0m}$to 3 m, these
74 figures are -0.5 ^{o}C and +10 W m^{-2}. In other words, the dependence of the surface temperature and
75 sensible heat flux on the roughness length is significant and highly non-linear. *Kim and Hong*
76 [2010] found that, using a more sophisticated representation of the roughness length as opposed
77 to the commonly used Charnock formula [*Charnock*, 1955], the Weather Research and
78 Forecasting [WRF, *Skamarock et al.*, 2008] model biases over the East Asian summer monsoon
79 are reduced. *Menut et al.* [2013] investigated the sensitivity of mineral dust emission fluxes over
80 northern Africa using satellite-derived roughness length and soil texture estimates. They found
81 that, with the new WRF configuration, the model is able to accurately reproduce the main dust
82 sources and the aerosol optical depth variability in the region. By using an updated zero-
83 displacement plane and aerodynamic roughness length values, roughly three times larger than the
84 default considered in WRF, for a sea breeze event in Tokyo in September 2011, *Varquez et al.*
85 [2015] reported a much improved simulation of the near-surface horizontal wind speed. *Jee et al.*
86 [2016] stressed that the use of a realistic roughness length over Seoul leads to an improvement of
87 the friction velocity, wind speed, temperature and relative humidity predictions, and ultimately
88 the model precipitation and Planetary Boundary Layer (PBL) depth forecasts. *Dong et al.* [2018]
89 highlighted the need to properly set up the surface roughness length according to the actual
90 vegetation type, for the WRF model to successfully simulate the surface and near-surface fields
91 in an Arctic coastal region. More recently, *Campbell et al.* [2019] have shown a significant
92 impact of an updated aerodynamic roughness length on meteorological parameters such as the
93 10-meter horizontal wind speed, 2-meter air temperature, and 2-meter mixing ratio, for different

land use categories over the United States. The papers referred above highlight the important role of the surface roughness length, not just on the prediction of surface and near-surface fields, but also on the forecast of the PBL depth.

The present study addresses the estimation of the aerodynamic roughness length over a bare-soil surface using eddy-covariance measurements made available during the UAE Rain Enhancement Program (UAEREP) Project [*Nelli et al.*, 2020]. The z_{0m} for each type of land-surface can be estimated from field measurements made for that particular surface, and is known to exhibit temporal variability on both monthly and diurnal time-scales [e.g. *D Zheng et al.*, 2013]. There are estimates of z_{0m} for a bare-soil surface only for a few locations outside the UAE, all based on in-situ and remote sensing data [e.g. *Marticorena et al.*, 2004; *Prigent*, 2005; *K Yang et al.*, 2008]. *Marticorena et al.* [2004] estimated the surface roughness over North Africa from satellite measurements. An empirical relationship between the observed bidirectional reflectance of the satellite data and roughness estimates from in-situ measurements [*Greeley et al.*, 1997] and from the geomorphological maps [*Marticorena et al.*, 1997] was derived, and subsequently applied to North Africa. Using this empirical relation, the z_{0m} value derived for Western Sahara and Arabian Peninsula regions is nearly 1 mm. A limitation of this method is the high sensitivity of the observations to clouds as well aerosols in the atmospheric column. *Prigent* [2005] made global estimations of z_{0m} for arid and semi-arid regions by using observations from the wind scatterometer onboard European Remote Sensing (ERS) satellite operating at 5.25 GHz. A statistical relationship is derived between the ERS scatterometer backscattering coefficients and quality in situ and geomorphological z_{0m} estimates. Based on this parameterized approach, the major deserts in North Africa, Arabia, and Asia, have roughness lengths below about 0.2 mm In addition to satellite-based methods, the surface roughness length

117 can also be computed from in situ-based approaches. For example, *K Yang et al.* [2008]
118 estimated z_{0m} from observed eddy-covariance measurements during the Heihe River Basin Field
119 Experiment (HEIFE, 1990-92) in an arid river basin in north-western China. Assuming that the
120 Monin-Obukhov similarity theory holds, the major features of the turbulent heat transfer are first
121 estimated, with the roughness length then computed from the logarithmic wind profile for both
122 neutral and nonneutral conditions. The optimal z_{0m} values for the Gobi (absolutely flat) and
123 Desert (sand dunes) flux sites are found to be roughly 0.68 and 2.74 mm, respectively. *Cullen et*
124 *al.* [2007] also calculated the roughness length over the top of Mount Kilimanjaro in Tanzania
125 using the logarithmic wind profile, even though in this case highly stable and unstable conditions
126 were excluded. z_{0m} was found to be 1.7×10^{-3} m, in line with estimated values over snow and ice.
127 For different sites in western Germany, *Graf et al.* [2014] estimated z_{0m} from single-level eddy-
128 covariance data using three distinct methods: (i) directly from the logarithmic wind profile; (ii)
129 as (i) but using a regression approach, which accounts for the non-linearity in Ψ_m, the integrated
130 universal momentum function; (iii) flux-variance similarity approach. The authors stressed the
131 need to compare the results of different methods, taking for example the ensemble mean or
132 median of the results, after excluding those that produce outliers, in order to have more robust
133 estimates. *Lu et al.* [2009] estimated z_{0m} indirectly by minimizing the cost function between the
134 friction velocity and that estimated using the logarithmic wind profile around Beijing, China.
135 The surface roughness length is found to be wind-direction dependent, with values in the range
136 0.001 to 0.01 m. *Prueger et al.* [2004], used the flux-variance similarity approach to estimate the
137 roughness length at a semi-arid site in New Mexico, US. It was found to range from 0.01 m at a
138 grass site to 0.025 m at sites with a slight topography. In this work, the aerodynamic roughness
139 length is first estimated using long-term eddy covariance measurements at one particular site in

the UAE, with the new value ingested into the WRF model which is then run over two months, in the warm and cold seasons. To the authors' knowledge, this is the first attempt to infer roughness length from in situ observations in the Arabian Peninsula the determined roughness length was then used WRF to assess its impact on the surface and near-surface model predictions in such a hyper-arid region. We analyze the inferred roughness length value with respect to values proposed in the literature and investigate the sensitivity of WRF to this critical parameter. We expect that the roughness length that is inferred from in situ observations using an eddy covariance station should be more representation of local surface condition and therefore lead to an improvement in the model performance.

This paper is organized as follows. Section 2 describes the WRF experimental setup and configuration. The estimation of the aerodynamic roughness length using eddy covariance measurements is discussed in section 3, while in section 4 the focus is on the impact of the updated roughness length on the surface and near-surface meteorological parameters over the UAE. In section 5, the WRF performance is evaluated against in-situ weather station data, with a summary of the main results presented in section 6.

2. Experimental Setup and Verification Diagnostics

The WRF [*Skamarock et al.*, 2008] model version 3.8.1 dynamical solver, with three-way interactive domains of grid sizes of 12 km, 4 km and 1.333 km shown in *Figure 1(a)*, is used to simulate the impact of an updated roughness length for the barren and sparsely vegetated land-cover category, the dominant land use type over the UAE as shown in *Figure 1(b)*. The outermost domain extends over the Arabian Peninsula, the Arabian Gulf, and Sea of Oman (d01; ~16.4^{o} – 31.4^{o} N, 46.3^{o} – 61.7^{o} E). The first nested domain covers the entire UAE region (d02;

163 ~20.7° – 27.3° N, 50.1° – 57.6° E), whereas the innermost grid is centered on Al Ain (d03; ~23.7°

164 – 24.9° N, 55.0° – 56.3° E).

165

166 (a) (b)

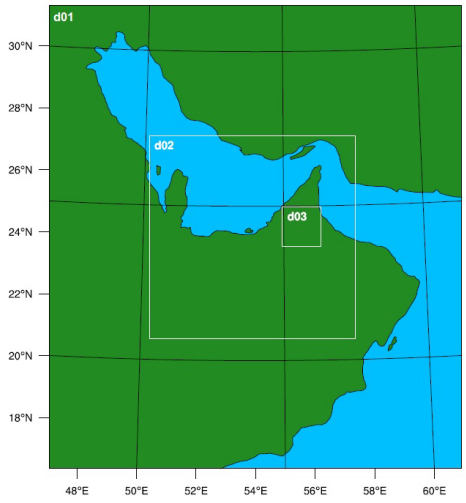

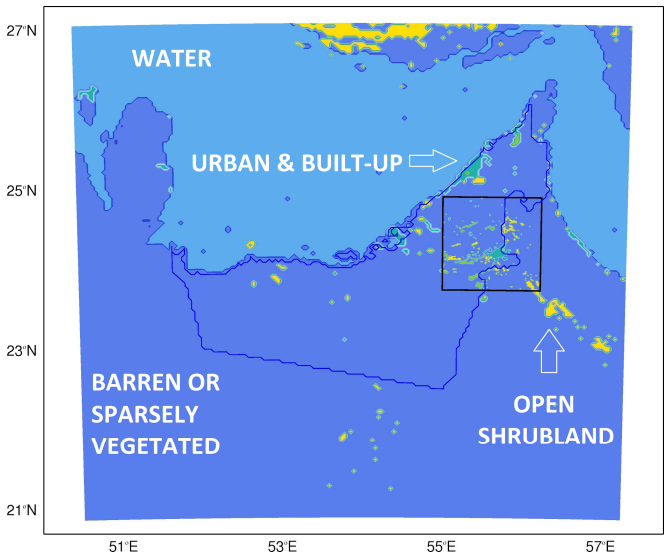

167

(c)

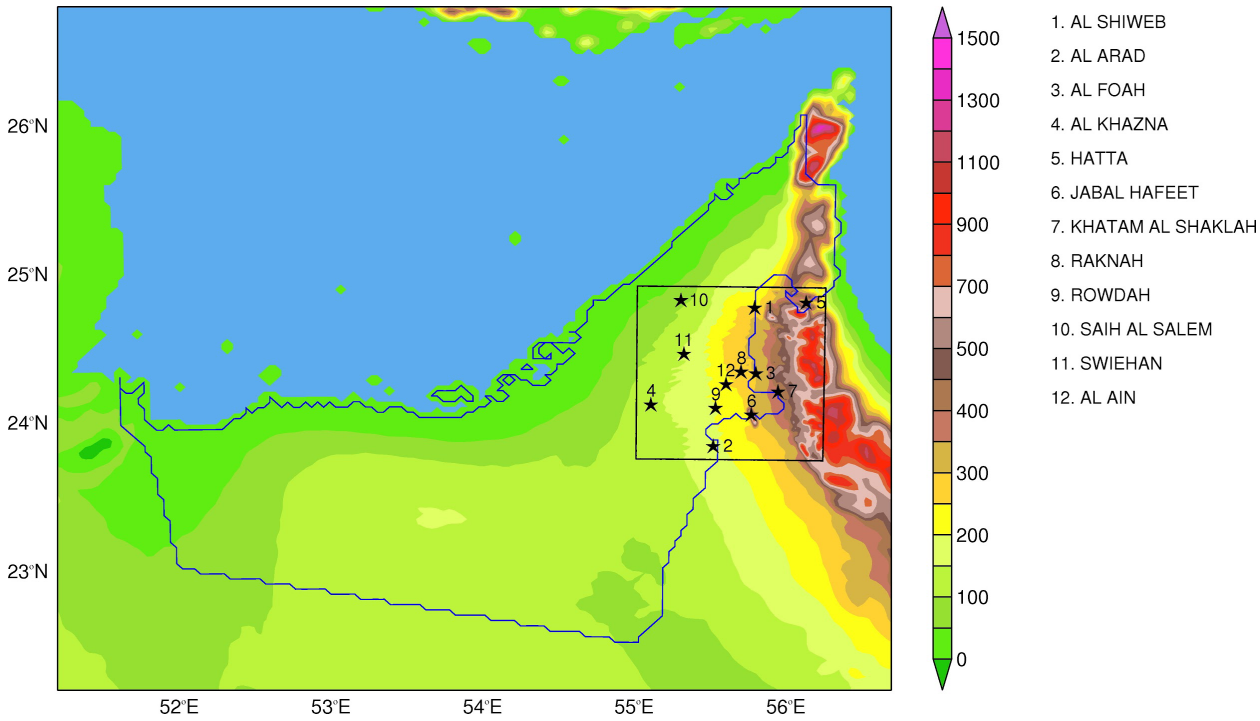

Figure 1. (a) Spatial extent of the 12 km (d01), 4 km (d02) and 1.333 km (d03) domains used in the WRF simulations, (b) dominant land cover category in the 4 km (d02) and 1.333 km (d03) grids, and (c) orography (m) of 4 km (d02) and 1.333 km (d03) grids, and location of the 12 weather stations in the latter for which hourly meteorological data is available for evaluation. In (b) and (c), the black rectangle denotes the spatial extent of the innermost nest.

The model physics options chosen are given in *Table 1*. A similar set up was used in previous studies over the UAE [e.g. *Chaouch et al.*, 2017; *Weston et al.*, 2018]. For all simulations, the Thompson cloud microphysics scheme is used to represent the grid-scale water vapour, cloud, and precipitation processes [*Thompson et al.*, 2008]. The sub-grid-scale clouds are represented with the Kain–Fritsch scheme [*Kain and Fritsch*, 1990; *Kain*, 2004], with subgrid-scale cloud feedbacks to radiation accounted for following *Alapaty et al.* [2012]. The cumulus scheme is switched off in the 4 km and 1.333 km grids. The atmospheric radiative heating is calculated using the Rapid Radiative Transfer Model (RRTM) longwave radiation [*Mlawer et al.*, 1997] and RRTM for Global Circulation Models (RRTMG) shortwave radiation [*Iacono et al.*, 2008]

185 schemes. The exchanges of surface fluxes of momentum, heat and moisture between land and
186 atmosphere are determined using the Quasi-Normal Scale Elimination (QNSE) Planetary
187 Boundary layer (PBL) and surface layer schemes [*Sukoriansky et al.*, 2005]. The land surface
188 model (LSM) employed in the numerical simulations is the Noah LSM [*Chen and Dudhia*,
189 2001].

190

Domains (Spatial scale)	Three (12 km, 4 km, 1.333 km) with one-way interaction
Vertical levels	45, with top level at 50 hPa
Time step	60 s (12 km grid), 20 s (4 km grid) and 20/3 s (1.333 km grid)
Initialization data	NCEP-GFS analysis data at 0.25^{o} spatial resolution
Initialization time	06 UTC
Integration time	72 h
Land-use and land-cover	Moderate Resolution Imaging Spectroradiometer (MODIS)
Radiation (Shortwave)	Rapid Radiative Transfer Model for Global Circulation Models (RRTMG)
Radiation (Longwave)	Rapid Radiative Transfer Model (RRTM)
Land Surface Model (LSM)	Noah LSM, with four soil layers
PBL & Surface Layer schemes	Quasi-Normal Scale Elimination (QNSE)
Microphysics parameterization	Thompson cloud microphysics scheme
Cumulus cloud parameterization	*12 km grid*: Kain-Fritsch (new Eta), with subgrid-scale cloud feedbacks to radiation switched on *4 km and 1.333 km grids*: No cumulus scheme

191

192 **Table 1.** Details of the model configuration used in the WRF simulations.
193

194 The land cover classes used in this work, *Figure 1(b)*, are estimated from the Moderate
195 Resolution Imaging Spectroradiometer (MODIS) measurements at 1 km spatial resolution for the

196 year 2001 [*Ran et al.*, 2010]. Following several field campaigns performed as part of the
197 UAEREP project, the soil texture and land use types are adapted to reflect their actual state. The
198 topography employed in the WRF simulations, downloaded from the model's website, is
199 carefully interpolated from a 30'' (or about ~925 m) spatial resolution dataset provided by the
200 United States Geological Survey (USGS). The land cover in the Noah LSM is composed of
201 twenty classes, and for each the roughness length is estimated using a predefined minimum and
202 maximum value given in *Table 2*. The linear interpolation is conducted on a monthly basis, with
203 the minimum z_{0m} corresponding to the minimum in vegetation coverage and vice-versa. For the
204 desert land cover type targeted in this work, z_{0m} is always set to 10 mm.

205

Land Cover Type	**Minimum z_{0m}(mm)**	**Maximum z_{0m}(mm)**
Evergreen Needleleaf Forest	500	500
Evergreen Broadleaf Forest	500	500
Deciduous Needleleaf Forest	500	500
Deciduous Broadleaf Forest	500	500
Mixed Forests	200	500
Closed Shurblands	10	50
Open Shrublands	10	60
Woody Savannas	10	50
Savannas	150	150
Grasslands	100	120
Permanent Wetlands	300	300
Croplands	50	150
Urban & Built-Up	500	500
Cropland/Natural Vegetation Mosaic	50	140

Snow and Ice	1	1
Barren or Sparsely Vegetated	**10**	**10**
Water	0.1	0.1
Wooded Tundra	300	300
Mixed Tundra	150	150
Barren Tundra	50	100

Table 2. Minimum and maximum aerodynamic roughness lengths, z_{0m} (mm), for each soil type used in the WRF simulations. The z_{0m} values for the land cover type targeted in this work, barren or sparsely vegetated, are highlighted in bold red font.

WRF is run for one month in the cold (February 2018) and warm (June 2018) seasons. The model is initialized with Global Forecast System (GFS) data at 0.25° spatial resolution every day at 06 UTC, with the output in the first 6 h forecast of each run regarded as spin-up and discarded. The boundary conditions are updated every six hours and each simulation is carried over for 72 h with a master time step of 60 s. The model output for each grid is stored hourly with that of the 4 km and 1.333 km grids used for analysis. The WRF predictions are evaluated against (i) 30-minute eddy-covariance measurements at Al Ain's International Airport (24°16'26.5535'' N; 55°37'03.2196'' E), taken as part of the UAEREP project [*Branch and Wulfmeyer*, 2019; *Nelli et al.*, 2020], and (ii) hourly station data at 12 sites over the country provided by the UAE's National Center of Meteorology (NCM), *Figure 1(c)*.

The WRF performance is assessed with the bias, equation (1), Mean Absolute Error (MAE), equation (2), and Root-Mean-Square Error (RMSE), equation (3), diagnostics. These scores, at the location of a given station X, are given by

$$BIAS(X,y) = \frac{1}{N}\sum_{i=1}^{N}[M(X,i) - O(X,i)] \quad (1)$$

$$MAE(X) = \frac{1}{N}\sum_{i=1}^{N}|M(X,i) - O(X,i)| \quad (2)$$

$$RMSE(X,y) = \sqrt{\frac{1}{N}\sum_{i=1}^{N}[M(X,i) - O(X,i)]^2} \quad (3)$$

where $M(X,i)$ is the WRF forecast at time i of the nearest grid point to the weather station X, $O(X,i)$ is the observed value at the same location, and N is the number of time-points considered. In addition, the Pearson's correlation coefficient, equation (4), is used to evaluate the similarity between the temporal evolution of the WRF-simulated wind speed and air temperature and that observed at each station. Here, $\overline{M}$ and $\overline{O}$ denote the means of $M(X,i)$ and $O(X,i)$ over all available times.

$$\rho(X) = \frac{\sum_{i=1}^{N}[M(X,i) - \overline{M}][O(X,i) - \overline{O}]}{\sqrt{\sum_{i=1}^{N}[M(X,i) - \overline{M}]^2}\sqrt{\sum_{i=1}^{N}[O(X,i) - \overline{O}]^2}} \quad (4)$$

3. Estimation of roughness length using eddy covariance measurements at Al Ain station

Eddy-covariance measurements from a micrometeorological tower installed in the premises of Al Ain's International Airport are used to estimate the aerodynamic roughness length, z_{0m} [*Nelli et al.*, 2020]. The terrain at the site is nearly homogeneous and obstacle free in the north-west and south-east directions, with major obstacles (namely buildings) located to the south and north-east.

242 Based on the Monin-Obukhov similarity approach, the mean wind speed in the surface
243 layer can be approximated by

244 $$U(z) = \frac{u_*}{\kappa}\left[\ln\left(\frac{z}{z_{0m}}\right) - \psi_m\left(\frac{z}{L}\right)\right] \quad (5)$$

245 where $U(z)$ is the near-surface horizontal wind speed (m s^{-1}), u_* is the friction velocity (m s^{-1}), L
246 is the Monin-Obukhov length, κ is the von Karman constant (=0.4), z is the measurement height
247 (here 2.3 m), and Ψ_m is the integrated universal momentum function. The horizontal wind speed
248 and u_* are estimated from ultrasonic anemometer measurements. This instrument is mounted on
249 top of a 2.3 m tower, and its data are archived at a 10 Hz sampling rate.

250 The surface layer stability is investigated through the Monin-Obukhov stability parameter
251 (z/L), where L is the Monin-Obukhov length, defined as

252 $$L = -\frac{u_*^3}{\kappa\frac{g}{\theta_v}\overline{\theta' w'}} \quad (6)$$

253

254 In equation (6), g is the acceleration due to gravity, w is the vertical velocity, θ is the potential
255 temperature, θ_v is the virtual potential temperature, $\overline{(\,)}$ denotes the time-mean and $(\,)'$ the
256 deviation from it. The z/L values in the range -0.01 < z/L < 0.01 represent the near neutral
257 stability regime, while z/L < -0.01 and z/L > 0.01 indicate unstable and stable regimes,
258 respectively [*Li et al.*, 2011]. According to *Paulson* [1970], for the unstable surface layer
259 condition, the universal momentum function Ψ_m is defined as

$$\Psi_m\left(\frac{z}{L}\right) = ln\left[\frac{1+x^2}{2}\left(\frac{1+x}{2}\right)^2\right] - 2\,arc\,tan(x) + \frac{\pi}{2} \quad (7)$$

with $x = [1 - \gamma(z/L)]^{1/4}$, where γ is a universal constant set to 19.3 [*Högström*, 1988]. For moderately stable conditions ($0.01 < z/L < 1$), Ψ_m is defined as

$$\Psi_m(z/L) = -\beta(z/L) \quad (8)$$

where $\beta = 6$ is another universal constant derived from experimental data.

Using equation (5), the aerodynamic roughness length, z_{0m}, can be estimated from the observed surface wind speed, u_*, and L. Following *Graf et al.* [2014] the outliers are filtered out by applying two conditions to the data, namely horizontal wind speed $U > 1.5$ ms^{-1} and $u_* > 0.05$ ms^{-1}. The measurements collected during the period April – October 2017 and February 2018 – January 2019 are used in the present study.

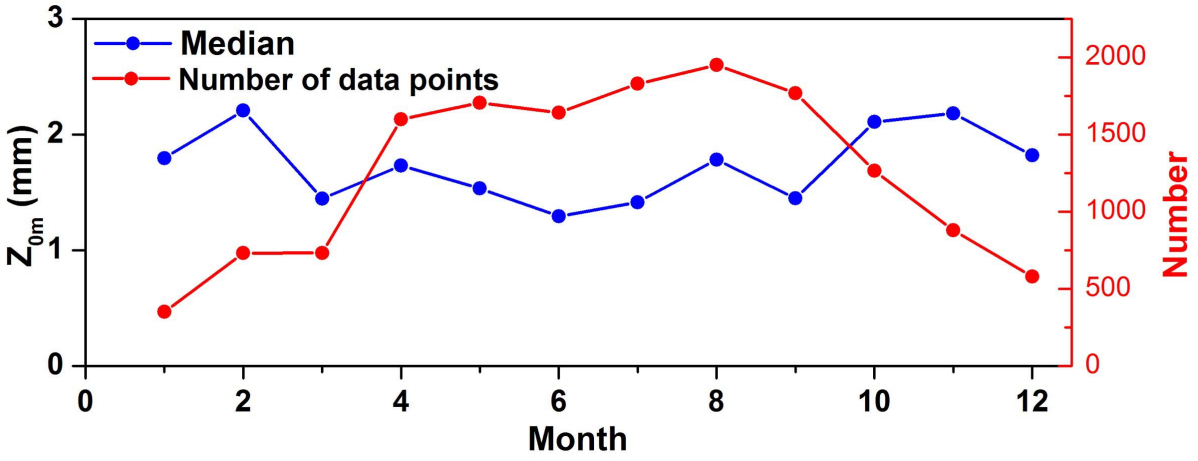

Figure 2. Median (blue) of aerodynamic roughness length (mm) as function of the month of the year. The red curve shows the number of data points used in the calculation of the diagnostics.

Table 3 shows the monthly mean wind speed U, frictional velocity u_*, median roughness length z_{0m} and number of data points used in the computation of the three quantities. Following

275 *Graf et al.* [2014], *Jesan et al.* [2016] and *Cullen et al.* [2007], the median roughness length is
276 selected instead of the mean value, as it is deemed more representative of the actual z_{0m}. All four
277 variables show very little monthly variability, with mean wind speeds in the range 3-4 m s^{-1} and
278 friction velocities mostly between 0.18 and 0.23 m s^{-1}, while the roughness length values vary
279 from 1.3 mm in June to 2.2 mm in November and February. These z_{0m} values are within the
280 range of the values cited in the literature for bare-soil surfaces, 0.2 – 2.74 mm [e.g. *Marticorena*
281 *et al.*, 2004; *Prigent*, 2005; *K Yang et al.*, 2008]. A comparison with *Table 2* reveals that the
282 estimated roughness length is roughly one order of magnitude smaller than the default value used
283 in WRF.

284

Month	**Wind speed (m s^{-1})**	**Frictional velocity (m s^{-1})**	**Median roughness length (mm)**	**Number of data points**
January	3.2	0.185	1.8	350
February	3.4	0.200	2.2	731
March	3.6	0.206	1.4	732
April	3.8	0.217	1.7	1598
May	4.0	0.229	1.5	1706
June	4.0	0.226	1.3	1641
July	3.8	0.217	1.4	1829
August	3.6	0.211	1.8	1950
September	3.7	0.205	1.4	1768
October	3.4	0.199	2.1	1265
November	3.4	0.202	2.2	878
December	3.0	0.177	1.8	579

285

286 **Table 3**. Monthly mean wind speed (m s^{-1}), frictional velocity (m s^{-1}), aerodynamic roughness length (mm; median),
287 and number of data points for the period April – October 2017 and February 2018 – January 2019.

288

289 In addition to a direct impact on the horizontal wind speed, equation (5), a change in the
290 surface roughness length will have an effect on the surface exchange coefficients. The exchange
291 coefficient for heat, C_h, can be expressed as

$$C_h = \frac{\kappa^2}{\left[ln\left(\frac{z}{z_{0m}}\right) - \psi_m\left(\frac{z}{L}\right)\right]\left[ln\left(\frac{z}{z_{0m}}\right) - \psi_h\left(\frac{z}{L}\right)\right]} \quad (9)$$

292

293 where $\psi_m$and $\psi_h$are the integrated similarity functions for momentum and heat, defined in
294 *Jiménez et al.* [2012]. A decrease in z_{0m}, with all other parameters being the same, will lead to a
295 lower C_h, which will have an impact on sensible heat flux, H. In the Noah LSM, the latter is
296 given by

$$H = \rho\, c_p\, C_h U(T_{SK} - T_{AIR}) \quad (10)$$

297

298 where ρ is the surface air density (kg m^{-3}), c_p is the specific heat capacity of the air at constant
299 pressure (J kg^{-1} K^{-1}), T_{SK} is the surface temperature (K), and T_{AIR} is the surface air temperature
300 (K), estimated from the air temperature on the lowest model level assuming that the potential
301 temperature is vertically well-mixed just above the surface. A reduced $C_h$will therefore lead to a
302 reduced H. The surface energy budget can be expressed as

$$\begin{aligned} R_n - G &= [SW\downarrow + LW\downarrow - SW\uparrow - LW\uparrow] - G \\ &= \left[SW\downarrow \times (1-\alpha) + LW\downarrow - \varepsilon\sigma T_{SK}^4\right] - G = H + LE \quad (11) \end{aligned}$$

303

where R_n is the net radiation flux, given by the sum of the downward (↓) and upward (↑) long-wave (LW) and short-wave (SW) radiation fluxes, LE is the latent heat flux, G is the ground heat flux, α is the surface albedo, ε is the surface emissivity, and σ is the Stefan-Boltzmann constant ($5.67 \times 10^{-8}\, Wm^{-2}K^{-1}$). In the Noah LSM, the surface temperature, T_{SK}, is obtained from equation (11). If H is reduced, T_{SK} will increase, so as to keep the surface energy budget closed. Hence, a decrease in z_{0m} is expected to lead to an increase in the near-surface horizontal wind speed U, equation (5), a decrease in the sensible heat flux H, equation (10), and an increase in surface temperature T_{SK}, equation (11).

4. WRF Sensitivity to Changes in Roughness Length

In this section, the WRF-predicted surface parameters in the simulations with the default and updated roughness lengths are discussed. The focus will be on the horizontal wind speed, surface temperature and sensible heat flux, fields that have been shown to be sensitive to the surface roughness length [e.g. *Kim and Hong*, 2010]. *Figure 3* shows the WRF predictions, as given by the 4 km and 1.333 km grids, for the horizontal wind for the cold (February) and warm (June) season months, and for the control configuration (left column) and the difference between the simulations with the updated (2.2 mm for February and 1.3 mm for June) and default (10 mm) roughness lengths (right column). The results are given at roughly the time of minimum (19 UTC or 23 local time, LT; nighttime) and maximum (13 UTC or 17 LT; daytime) diurnal wind speed.

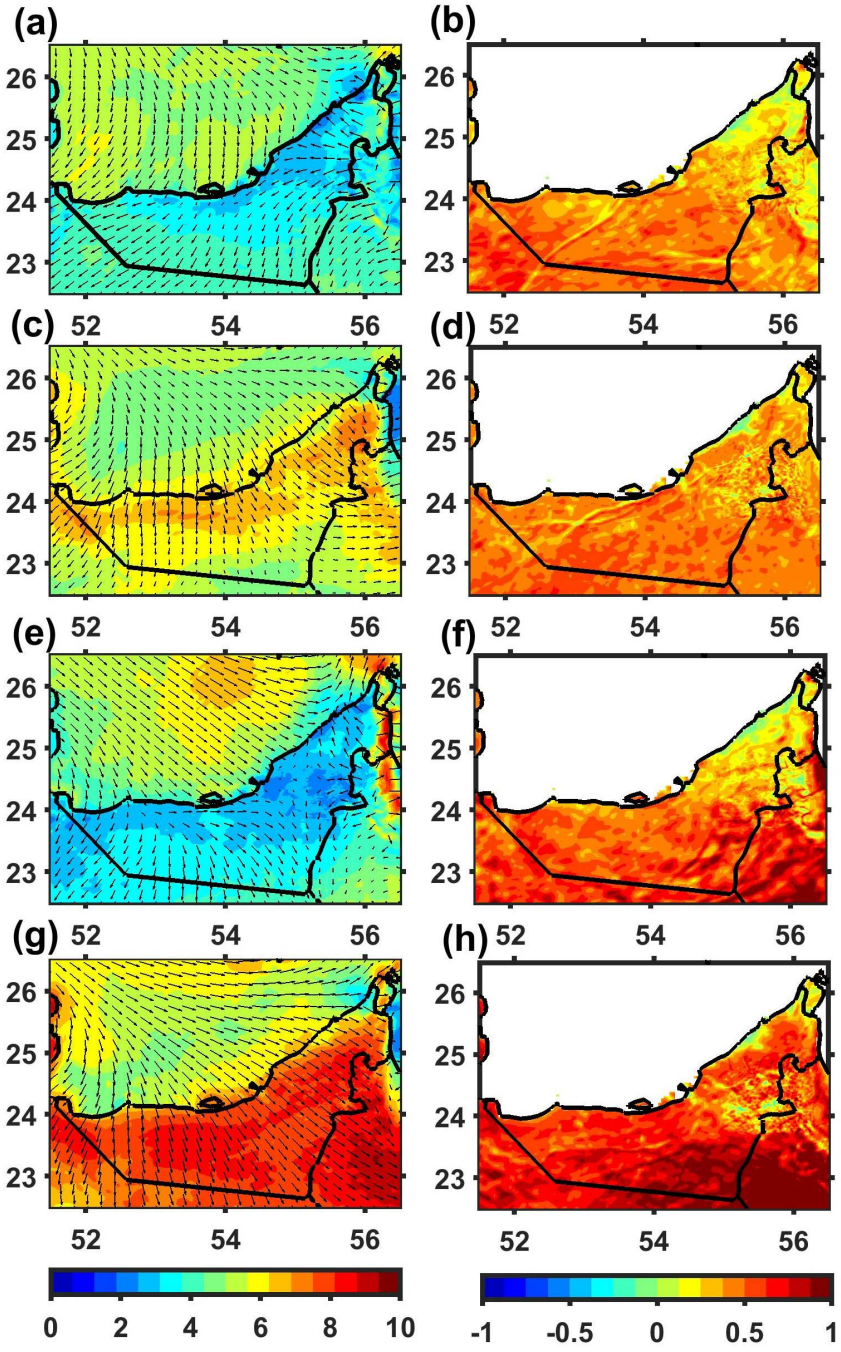

Figure 3. Horizontal wind speed (m s^{-1}) for the (a) WRF control configuration, and (b) horizontal wind speed difference between modified and control runs for February 2018 at 19 UTC or 23 LT (nighttime). (c)-(d) are as (a)-(b) but for daytime (13 UTC or 17 LT). (e)-(h) are as (a)-(d) but for June 2018. The results shown here are for the 4 km and 1.333 km grids.

The left panels in *Figure 3* show the horizontal wind speed for a typical winter and summer month over the UAE. For both seasons, there is a stark contrast between the land and the

adjacent Arabian Gulf: while during daytime the wind is stronger in the former, in association with the sea-breeze circulation reinforced by the background north-westerly winds, at night the highest magnitudes are predicted over the latter, which can be explained by the land breeze circulation [*Eager et al.*, 2008]. By and large, the near-surface wind speed is slightly stronger in June when the sea-breeze circulation is more intense and occurs more frequently, even though in both seasons it has a magnitude between roughly 5 and 10 m s^{-1}, in line with published work [e.g. *Zhu and Atkinson*, 2004; *Eager et al.*, 2008; *Naizghi and Ouarda*, 2017]. It is interesting to note that, on the eastern side of the country right next to the Al Hajar mountains, the horizontal wind speed is much lower during daytime in both months, as seen by the blue shading in (c) and (g). Here, the sea and land-breeze circulations are mostly controlled by the Sea of Oman and not by the Arabian Gulf, and may not be as vigorous, a conclusion also reached by *Yagoub* [2010]. The difference plots look remarkably similar for both seasons, with an expected increase in the strength of the wind, following equation (5), by roughly 0.5 to 1 m s^{-1} over the regions where the roughness length is modified (cf. *Figure 1(b)*); elsewhere the differences are negligible. This strengthening of the near-surface wind is more significant during daytime when the wind speeds are higher. *Reijmer et al.* [2004] reported that, when the aerodynamic roughness length was reduced from 3 to 10^{-3} m over Antarctica, the horizontal wind speed changed by ±2 m s^{-1}. Over southern China, *Wang et al.* [2009] found a decrease of the wind speed of up to 3 m s^{-1} when the roughness length was increased by roughly two orders of magnitude, due to the urbanization of the region. It is possible then that a change in the roughness length by an order of magnitude in a hyper-arid region, considered in this work, gives a wind speed difference of roughly 0.5 to 1 m s^{-1}.

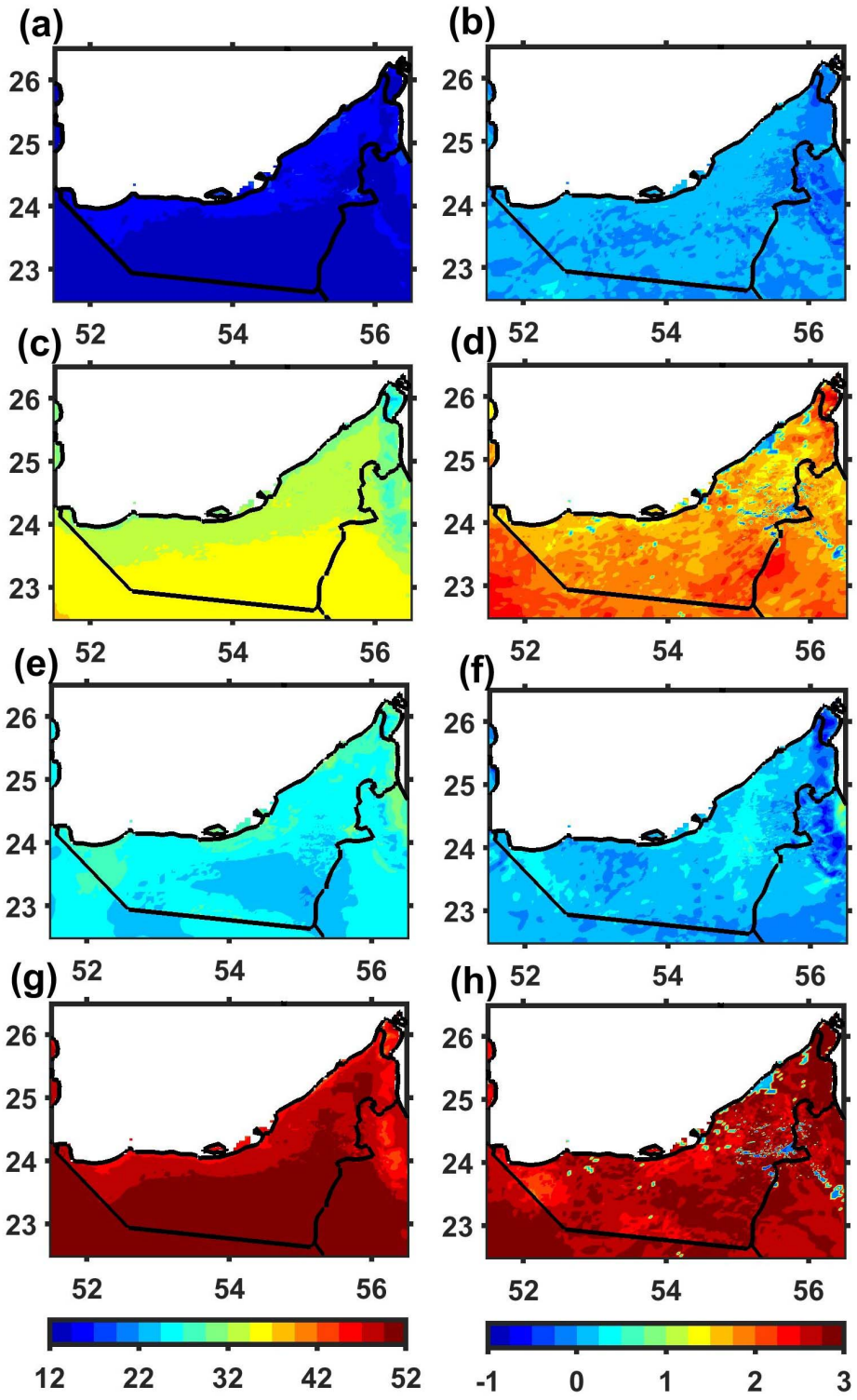

Figure 4. As *Figure 3* but for surface temperature (ºC). The times shown are 03 UTC or 07 LT (a-b) and 10 UTC or 14 LT (c-d) for February 2018, and 01 UTC or 05 LT (e-f) and 09 UTC or 13 LT (g-h) for June 2018, when the skin temperature is minimum and maximum, respectively.

357 *Figure 4* is as *Figure 3* but for the surface/skin temperature. The mean values for the
358 daytime and nighttime temperatures, left column, are in line with those reported in the literature
359 [e.g. *Komuscu*, 2017]. As expected, coastal locations exhibit a smaller amplitude temperature
360 diurnal cycle compared to inland sites, with cooler daytime and warmer nighttime temperatures,
361 due to the moderating influence of the Arabian Gulf [e.g. *Zhu and Atkinson*, 2004]. This is
362 reflected by the negative surface temperature gradient from coastal to inland regions at night, and
363 positive during daytime. In winter at night, and as a result of strong radiative cooling, surface
364 temperatures can drop to 12ºC, with fog formation being a regular occurrence [e.g. *Chaouch et*
365 *al.*, 2017; *Weston et al.*, 2018]. On the other hand, daytime surface temperatures in some inland
366 regions can exceed 50ºC, as a result of the excessive downward short-wave radiation flux arising
367 from a combination of clear skies and dry weather conditions. The sea surface temperature over
368 the Arabian Gulf ranges from 22ºC in winter to 32ºC in summer. When the roughness length is
369 updated in the model, the nighttime surface temperature stays about the same, with differences
370 generally within ±0.5ºC. However, the daytime temperature increases by roughly 1.5-2.5ºC. The
371 fact that a change in the surface roughness length has a significant impact on the maximum
372 temperature but a negligible influence on the minimum temperature is consistent with other
373 studies such as *June et al.* [2018]. This is the case because an updated roughness length will
374 affect the surface temperature through changes in the radiative heat fluxes and subsequently in
375 the surface energy budget, equations (9)-(11). As the heat fluxes are rather small at night [See
376 Figure 5 in *Nelli et al.*, 2020], the surface temperature is roughly the same in the two simulations.
377 In terms of magnitude, *June et al.* [2018] reported a roughly 1ºC increase in air temperature for a
378 doubling of the roughness length in Indonesia, whereas *Reijmer et al.* [2004] found an air
379 temperature change of up to ±10ºC for a roughness length reduction from 3 to 10^{-3} m over

380 Antarctica. For a vegetated site in the Netherlands, *Giorgi* [1997] noted a decrease in surface
381 temperature by about 0.4ºC when the roughness length was increased from 0.15 to 0.4 m, while
382 an increment of z_{0m} to 3 m changed the surface temperature by roughly 0.5ºC. The magnitude of
383 the surface temperature difference given in *Figure 4* is therefore in line with that reported by
384 other authors, larger than that of *Giorgi* [1997] given the hyper-arid climate of the UAE and
385 consequent lack of vegetation.

386

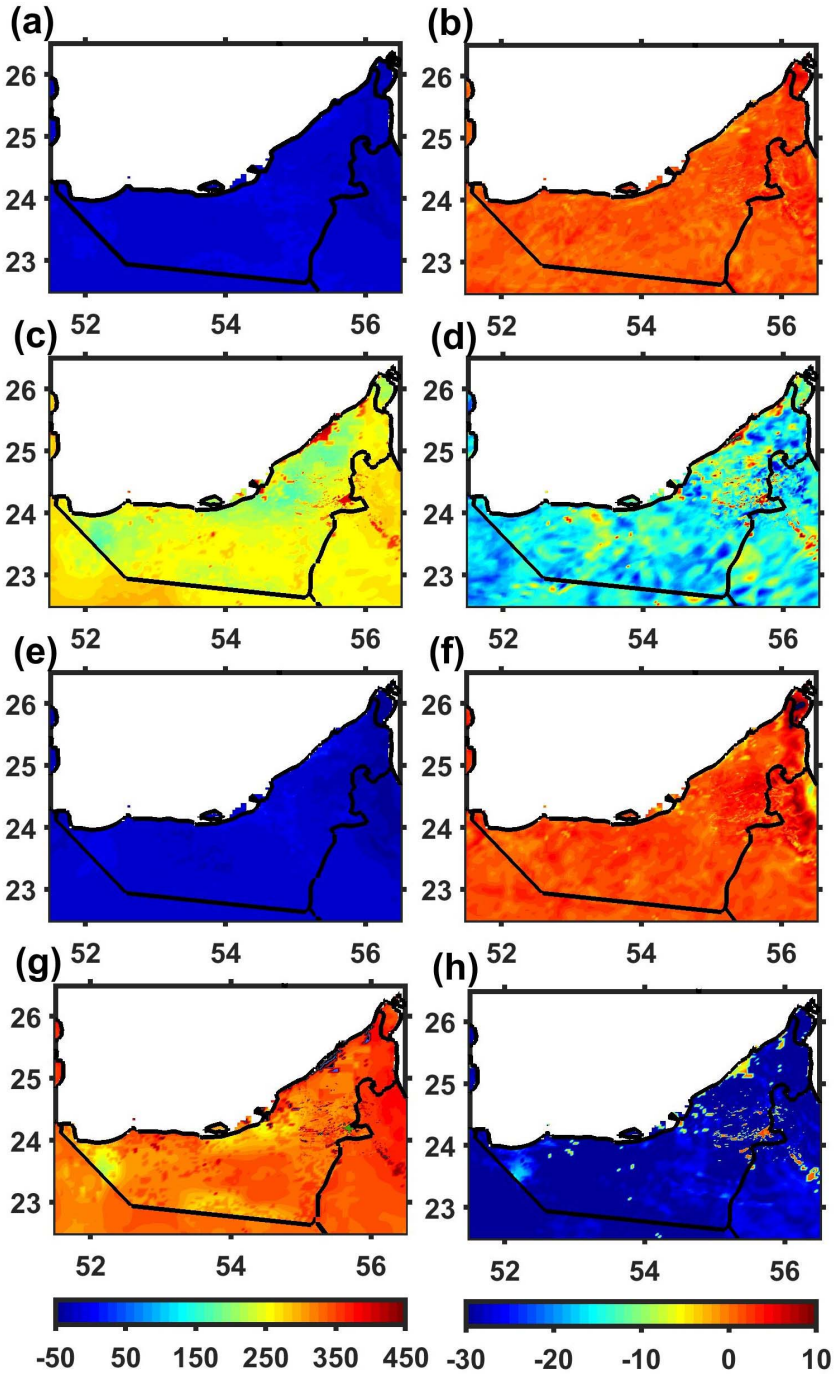

387

388 **Figure 5.** As *Figure 3* but for the sensible heat flux (W m^{-2}). The times shown are 03 UTC or 07 LT (a-b) and 10
389 UTC or 14 LT (c-d) for February 2018, and 01 UTC or 05 LT (e-f) and 09 UTC and 13 LT (g-h) for June 2018,
390 when the skin temperature reaches its minimum and maximum values, respectively.

391

The final field shown is the sensible heat flux, H, given in *Figure 5*. The mean values for the daytime and nighttime fluxes, left column, are in line with those reported e.g. in *Nelli et al.* [2020]. At night, the fluxes are close to zero or even negative indicating the presence of an inversion, whereas during daytime they are mostly in the range 150 to 350 W m^{-2} in winter and 250 to 450 W m^{-2} in the summer. It is interesting to note that over the urban regions (cf. *Figure 1(b)*) the sensible heat flux values are rather large during daytime, in excess of 450 W m^{-2} in the summer season. These H values are high but not unprecedented: e.g. *Man Sing et al.* [2015] reported that in central business districts of Hong-Kong, the sensible heat flux can exceed 1000 W m^{-2}, higher than the surface net radiation flux. As H is rather small at night, the changes in the magnitude of the sensible heat flux when the roughness length is updated will be negligible. During daytime, however, a reduction of the roughness length by roughly an order of magnitude, and in line with equations (10)-(11), leads to a decrease in H, by roughly 5 to 10 W m^{-2}. *Reijmer et al.* [2004] found a change in H of 20-35 W m^{-2} when the roughness length was varied by roughly three orders of magnitude over Antarctica. *Giorgi* [1997] reported that H increased by about 4 W m^{-2} when $z_{0m}$was increased from 0.15 to 0.4 m over Cabaux in the Netherlands, but a further increase of the roughness length to 3 m led to a rise in H by roughly 10 W m^{-2}. The magnitude of the change in H found here is therefore consistent with that reported in the referred studies.

5. Evaluation of WRF simulations using observational data

In the previous section, the impact of a modification of the roughness length on the near-surface wind speed, surface temperature and sensible heat flux over the UAE for a winter and

summer month was discussed. Here, the performance of the two WRF configurations is assessed against eddy covariance data at the Al Ain site where the roughness length estimation took place, and the 12 NCM stations shown in *Figure 1(c)*.

Figures 6 and *7* show the time-series of the three variables at Al Ain for February and June 2018. The left panels show the data for the full month, and the right panels give the WRF biases for the simulations with the control and modified configurations.

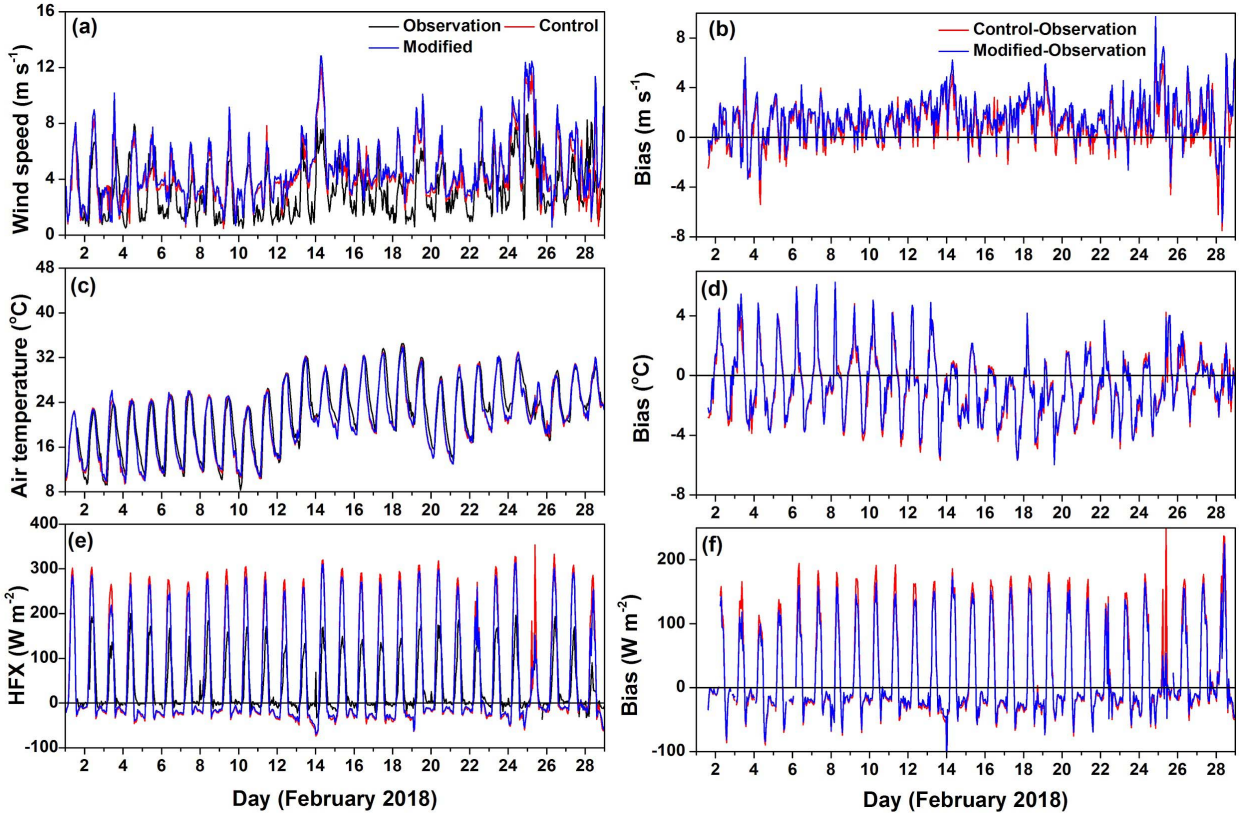

Figure 6. (a) Observed (black) and WRF-predicted 10-meter horizontal wind speed (m s^{-1}) for the simulations with the control (red) and modified (blue) configurations for February 2018 at Al Ain location. (c) and (e) are as (a) but for the 2-m air temperature (°C) and sensible heat flux (HFX, positive if upwards from the surface; W m^{-2}), respectively. (b), (d) and (f) show the correspondent WRF biases.

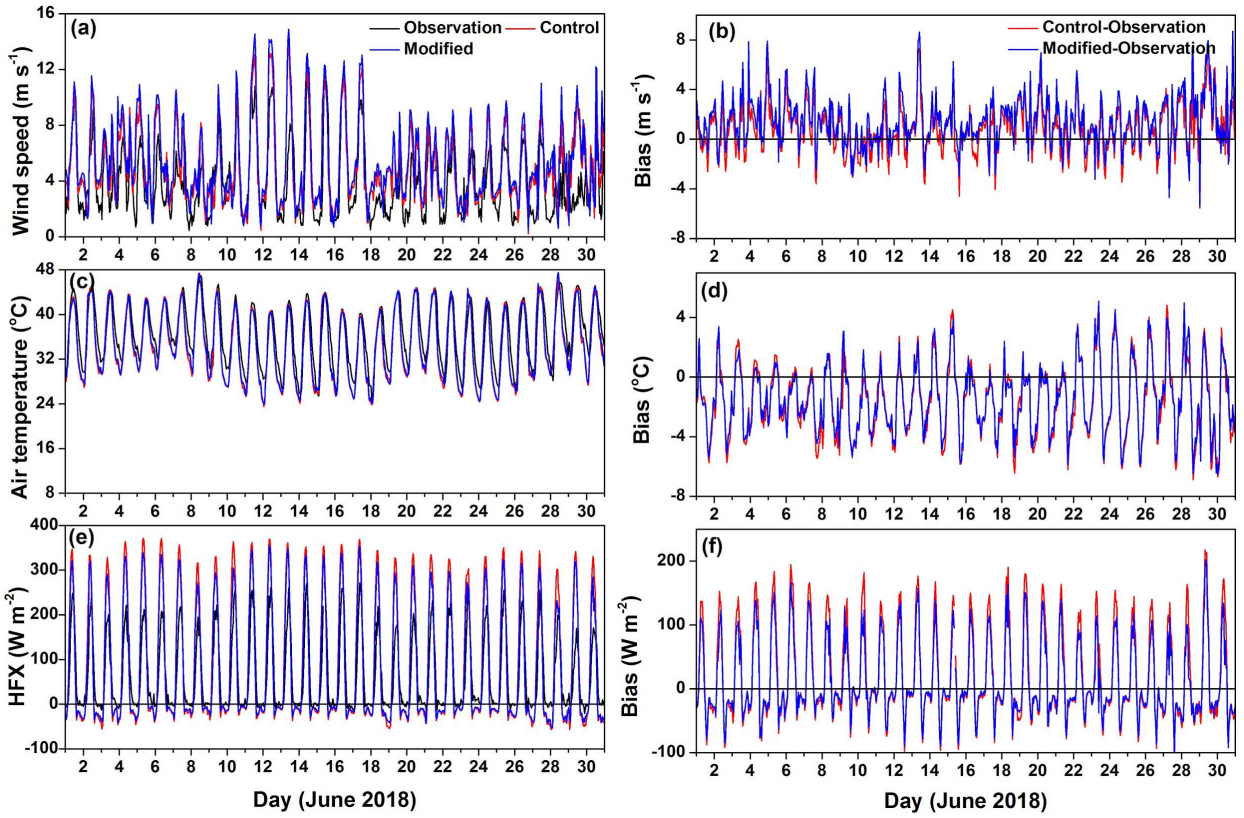

Figure 7. As *Figure 6* but for June 2018.

For February 2018, the wind speed at Al Ain was generally low, not exceeding 8 m s^{-1}. In line with *Nelli et al.* [2020], the wind speed diurnal cycle at Al Ain follows a bi-model distribution, with a primary peak in the evening hours, around 18-19 LT, and a secondary peak in the early morning, around 8-9 LT. They result from the interaction of the land/sea-breeze circulation with the topographic-driven winds that arise from the presence of the nearby Al Hajar mountains. The first 11 days were rather cool, with daytime maximum temperatures generally below 25ºC and nighttime minimum temperatures at times below 10ºC. In the second half of the month, however, it was much warmer, in particular at night, with minimum temperatures above 20ºC in the last days. The large (>100 W m^{-2}) sensible heat fluxes during the day, driven by the strong heating of the land surface by the Sun, contrast with the rather small or even negative values at

438 night, the latter an indication of the presence of an inversion. By and large, WRF over predicts
439 the strength of the near-surface winds typically by 1-3 m s^{-1}, with slightly larger biases when the
440 surface roughness length is updated (maximum differences of ±2 m s^{-1}), in line with *Figure 3*.
441 The tendency of the WRF model to overestimate the 10-meter horizontal wind speed in arid
442 regions has been highlighted by other authors such as *Gunwani and Mohan* [2017], who also
443 reported similar biases. *Hari Prasad et al.* [2016] in a tropical station in southeast India, *Cheng*
444 *and Steenburgh* [2005] and *Steeneveld et al.* [2008] over the United States, and *Borge et al.*
445 [2008] over the Iberian Peninsula, also reached a similar conclusion. Possible explanations for
446 this systematic discrepancy include (i) a poor representation of its subgrid-scale fluctuations and
447 of the surface drag parameterization in the model; (ii) an inaccurate simulation of the land and/or
448 sea surface temperatures, and hence the low-level atmospheric circulation; (iii) uncertainties in
449 the estimation of the roughness length and measured wind speed; (iv) impact of unresolved
450 topography not accounted for in the WRF runs. In the first 14 days of the month, WRF exhibits a
451 clear tendency to overestimate the nighttime temperature, while in the second half, it is mostly
452 underestimated. These discrepancies are generally within ±2ºC, with the simulation with the
453 reduced roughness length giving an improved performance (the bias is generally reduced by up
454 to 2ºC), consistent with *Figure 4*. The larger bias values seen in *Figure 6(d)* arise from a
455 tendency of the WRF model to warm up faster in the morning and cool down faster in the
456 evening with respect to observations. This has been reported by *Weston et al.* [2018], and can be
457 explained by (i) an incorrect representation of the local topography, such as a topographic
458 orientation tilted more towards the Sun in the morning in WRF; (ii) an under prediction of the
459 amount of dust or greenhouse gas concentrations in the atmosphere, and/or (iii) deficiencies in
460 the radiation scheme. Given the referred biases in the temperature diurnal cycle, the sensible heat

461 flux variability will be exaggerated in the two WRF simulations. In particular, *H* is higher than
462 that observed during the daytime, owing to the warmer surface temperatures, and lower at night,
463 indicating a stronger inversion in the model. As for the temperature, when run with the modified
464 configuration, WRF generally gives more accurate sensible heat flux predictions, with a decrease
465 in the bias by up to 50 W m^{-2}.

466 The model biases highlighted above for the winter month (February 2018) are also
467 mostly present in the summer month (June 2018), as seen by comparing *Figure 6* with *7*. The
468 magnitude of the wind speed overestimation is slightly larger in the warm season, at times
469 exceeding 8 m s^{-1}. However, the wind speed in June 2018 is also generally higher than that in
470 February, in line with *Eager et al.* [2008] and *Nelli et al.* [2020] and *Figure 3*, due to the stronger
471 land/sea-breeze and downslope-upslope circulations of the nearby Al Hajar mountains. While in
472 February 2018 WRF both overestimated and underestimated the minimum temperature, in June
473 the latter tendency prevails throughout the month, also with respect to the maximum
474 temperatures. This cold bias has been reported by other authors in studies over arid and semi-arid
475 regions [e.g. *W Zheng et al.*, 2012; *Weston et al.*, 2018; *Valappil et al.*, 2019], and can at least be
476 partially corrected by modifying the land surface model's configuration [*Weston et al.*, 2018].
477 The diurnal variability of the observed sensible heat flux is comparable to that in the cold season,
478 except that the higher daytime surface temperatures lead to more positive fluxes during the day,
479 while at night temperature inversions are less frequent compared to the winter month. The
480 tendency of WRF to warm up too fast in the morning and cool down at a higher rate compared to
481 observations is also seen in *Figure 7*, as are the more skillful predictions of the modified
482 configuration for the air temperature and sensible heat flux.

In *Figures 6* and *7* the WRF predictions are assessed against the observed measurements at Al Ain. However, similar conclusions regarding the model's performance are drawn for the other sites for which in situ data is available for evaluation. As an example, *Figure 8* shows the model air temperature bias for the control simulation, and the difference between the predictions of the modified and control WRF runs, for stations 1 to 12, located in the 1.333 km grid, *Figure 1(c)*. For February 2018, the most significant bias is an over prediction of both the daytime and nighttime temperatures, while in June 2018 the biases are generally of a smaller magnitude, with a weak cold bias at night at the vast majority of the stations. For both months, the difference between the forecasts of the two WRF simulations generally has the opposite sign to the control WRF run bias, which indicates that the run with the modified configuration gives more skillful predictions. The magnitude of this improvement, however, is smaller than the bias of the control WRF run, not exceeding about 0.6 K. *Table 4* shows the bias, RMSE, MAE and correlation (ρ) diagnostics for the two months and simulations and all eight stations. When averaged over all times, the WRF air temperature biases are roughly the same for the two runs, generally within 0.1 K, even though the simulation with the updated roughness length tends to give the smallest values. The same is true for the RMSE and MAE scores, while the correlations, already high in the control simulation mostly in excess of 0.93, do not show much variability. *Figure 9* is as *Figure 8* but for the 10-m horizontal wind speed. For the control simulation, and for all stations considered, the largest biases occur around 12-14 UTC (16-18 LT), in the local evening time, when the wind speed is typically at the maximum. For stations 3-5, 8 and 11, there is another positive peak of a smaller amplitude in the morning, around the time of the secondary maximum. At other times the wind speed biases are small, except mainly for stations 6 and 12 where the wind strength is under predicted by WRF at night. At these stations, the wind speed is stronger,

generally exceeding 5 m s^{-1}, with the model predicting weaker winds than those observed. In other words, the model wind speed bias seems to be a function of the strength of the wind, which is further analyzed below. In line with *Figures 3*, *6* and *7*, and mostly in the evening hours, the positive biases are further augmented when the roughness length is reduced, but the negative biases are mitigated. The verification diagnostics given in *Table 4* reflect the discussion above: poorer bias, RMSE and MAE scores for the simulation with the reduced roughness length, and comparable correlation coefficients for the two runs, generally in excess of 0.65. The lower scores for the 10-m wind speed compared to the 2-m air temperature can be explained by the higher temporal variability of the latter, more dependent on local-scale conditions and hence harder to accurately simulate.

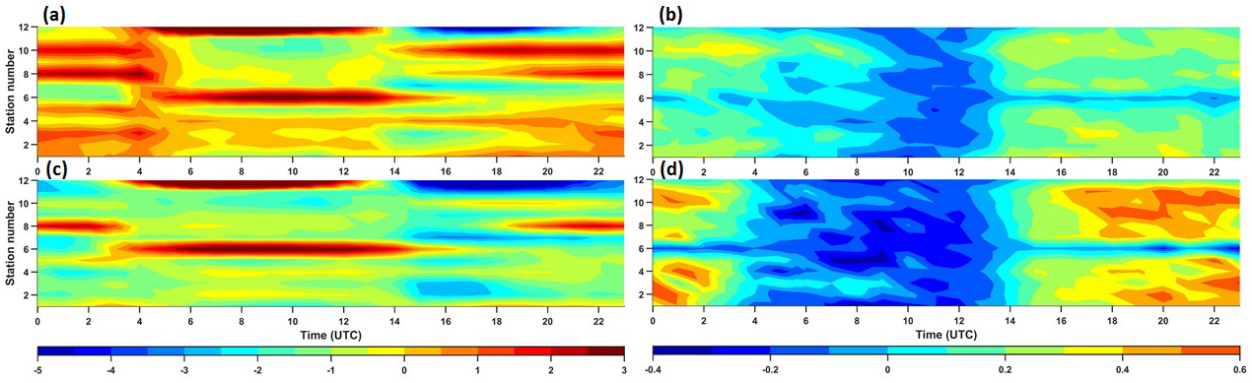

Figure 8. 2-m air temperature bias (K) with respect to the NCM station data for the control WRF configuration for (a) February 2018 and (c) June 2018. (b) and (d) show the difference between the predictions of the modified and control WRF configurations for the same period. The horizontal axis shows the time in UTC while the vertical axis gives the station number (see *Figure 1(c)* for more details).

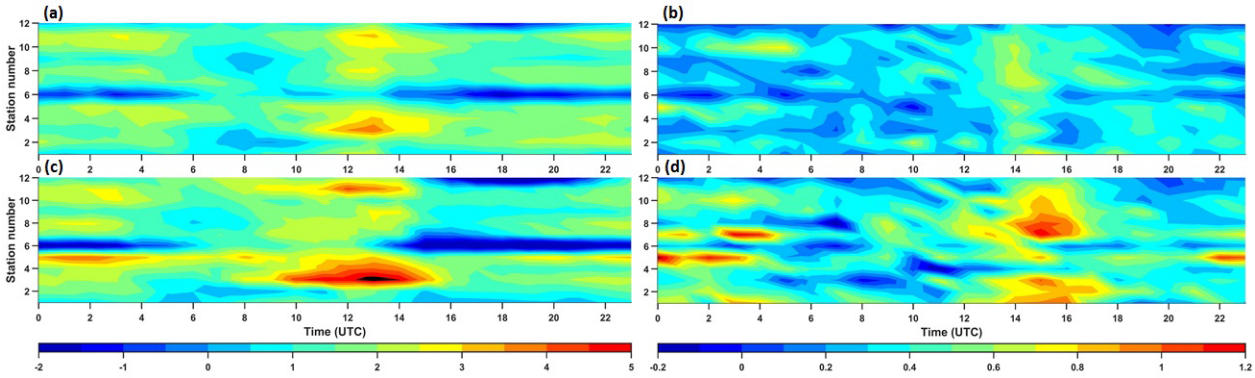

522

523 **Figure 9.** As *Figure 8* but for the 10-m horizontal wind speed (m s^{-1}).

524

Station Name (#)		10-m wind speed (m s^{-1})				2-m air temperature (^{o}C)			
		BIAS	MAE	RMSE	ρ	BIAS	MAE	RMSE	ρ
Al Shiweb (#1)	F	0.9 (1.3)	1.6 (1.8)	2.2 (2.5)	0.632 (0.613)	0.1 (0.3)	1.1 (1.2)	1.4 (1.6)	0.975 (0.97)
	J	0.7 (1.3)	1.7 (2.1)	2.5 (3.1)	0.612 (0.556)	-0.6 (-0.5)	1.3 (1.4)	1.6 (1.8)	0.97 (0.964)
Al Arad (#2)	F	1.5 (1.8)	1.8 (2.1)	2.2 (2.5)	0.657 (0.639)	0.1 (0.2)	1.1 (1.2)	1.5 (1.6)	0.975 (0.973)
	J	1.0 (1.5)	1.6 (2.1)	2.1 (2.5)	0.818 (0.786)	-1.3 (-1.1)	1.6 (1.5)	2.0 (1.9)	0.973 (0.973)
Al Foah (#3)	F	1.8 (2.0)	2.1 (2.3)	2.6 (2.9)	0.507 (0.497)	0.1 (0.2)	1.3 (1.4)	1.8 (1.8)	0.96 (0.959)
	J	2.6 (3.0)	2.8 (3.2)	3.6 (4.1)	0.399 (0.375)	-1.4 (-1.2)	1.8 (1.8)	2.2 (2.1)	0.956 (0.953)
Al Khazna (#4)	F	2.0 (2.3)	2.1 (2.4)	2.6 (3.0)	0.634 (0.597)	0.3 (0.4)	1.2 (1.2)	1.5 (1.6)	0.965 (0.963)

	J	2.1 (2.4)	2.2 (2.5)	2.8 (3.1)	0.755 (0.745)	-0.8 (-0.7)	1.1 (1.1)	1.5 (1.5)	0.98 (0.979)
Hatta (#5)	F	1.8 (2.1)	2.1 (2.4)	2.9 (3.3)	0.523 (0.493)	-0.4 (-0.3)	1.5 (1.5)	1.9 (2.0)	0.92 (0.915)
	J	2.8 (3.4)	3.0 (3.6)	3.7 (4.4)	0.568 (0.516)	-1.2 (-1.1)	1.7 (1.7)	2.0 (2.1)	0.933 (0.921)
Jabal Hafeet (#6)	F	-0.4 (-0.2)	2.4 (2.4)	2.9 (3.0)	0.505 (0.501)	0.8 (0.8)	2.0 (2.0)	2.4 (2.4)	0.88 (0.881)
	J	-1.0 (-0.7)	3.2 (3.3)	3.9 (4.0)	0.359 (0.338)	0.9 (0.8)	2.3 (2.2)	2.7 (2.6)	0.783 (0.790)
Khatam Al Shaklah (#7)	F	1.4 (1.7)	1.9 (2.1)	2.3 (2.7)	0.532 (0.516)	-1.2 (-1.1)	1.6 (1.5)	1.9 (1.9)	0.959 (0.96)
	J	1.4 (2.1)	2.0 (2.4)	2.7 (3.3)	0.669 (0.635)	-1.9 (-1.8)	2.2 (2.1)	2.5 (2.4)	0.954 (0.955)
Raknah (#8)	F	1.6 (1.9)	1.9 (2.1)	2.3 (2.6)	0.659 (0.663)	0.8 (0.9)	1.6 (1.7)	2.3 (2.5)	0.965 (0.962)
	J	1.7 (2.1)	2.0 (2.3)	2.4 (2.8)	0.797 (0.783)	0.1 (0.2)	1.7 (1.8)	2.1 (2.3)	0.964 (0.961)
Rowdah (#9)	F	1.0 (1.3)	1.5 (1.7)	1.9 (2.2)	0.701 (0.697)	-0.3 (-0.2)	1.0 (1.1)	1.4 (1.4)	0.978 (0.976)
	J	1.2 (1.7)	1.7 (2.0)	2.3 (2.7)	0.746 (0.739)	-1.4 (-1.3)	1.5 (1.4)	1.9 (1.7)	0.979 (0.980)
Saih Al Salem (#10)	F	1.7 (2.1)	1.9 (2.3)	2.4 (2.9)	0.63 (0.611)	0.8 (1.0)	1.9 (2.1)	2.4 (2.5)	0.969 (0.967)
	J	1.7 (2.1)	1.9 (2.3)	2.4 (2.9)	0.741 (0.705)	-0.9 (-0.7)	1.3 (1.4)	1.8 (1.9)	0.974 (0.969)
Swiehan (#11)	F	2.0 (2.4)	2.2 (2.4)	2.6 (2.9)	0.715 (0.72)	-0.8 (-0.6)	1.4 (1.5)	1.8 (1.8)	0.972 (0.971)

	J	2.1 (2.5)	2.3 (2.6)	2.9 (3.2)	0.700 (0.703)	-2.2 (-2.0)	2.2 (2.1)	2.6 (2.4)	0.979 (0.977)
Al Ain (#12)	F	0.3 (0.4)	1.8 (1.8)	2.3 (2.3)	0.335 (0.373)	0.6 (0.6)	4.0 (3.9)	4.9 (4.8)	0.592 (0.602)
	J	0.5 (0.7)	2.6 (2.6)	3.3 (3.4)	0.211 (0.243)	-0.2 (-0.2)	5.1 (5.0)	6.0 (5.9)	0.344 (0.359)

Table 4. Verification diagnostics for the 10-m wind speed and 2-m air temperature at the 12 NCM weather stations given in *Figure 1(c)*, for the control (modified) WRF configuration. The letters "F" and "J" denote the February 2018 and June 2018 months, respectively.

In order to analyze the dependence of the model's wind speed bias on the strength of the wind, *Figure 10* shows the bias for the 12 NCM stations, for the control and modified WRF configurations, and for the two months as a function of the wind speed. As can be seen, WRF has a tendency to overestimate the strength of low winds, in particular for speeds < 4 m s^{-1}, and underestimate the strength of winds for speeds mostly in excess of 6 m s^{-1}. This behaviour has been reported by other authors [e.g. *Carvalho et al.*, 2012; *Q Yang et al.*, 2013], and may be attributed to deficiencies in the PBL scheme. In particular, it is possible that the model under predicts the turbulent mixing for low winds and over predicts it for high winds. While for low wind speeds the model performance with the two configurations is comparable, with an overestimation of the observed values by around 2 m s^{-1}, for high speeds, in excess of roughly 6 m s^{-1}, the simulation with a reduced roughness length gives more skillful predictions, typically by 1-3 m s^{-1}. In other words, while when all wind speeds are taken into account the two WRF runs give comparable predictions, the improved configuration is more accurate for stronger winds, which are more critical for human and industrial activities [e.g. *Stathopoulos*, 2009]. An analysis of the results of domain 02 (4 km resolution) for the same set of stations revealed generally

higher biases of up to 3 m s^{-1} (not shown), highlighting the added value of having a higher-resolution grid over the target region for the simulation of the strength of the near-surface horizontal wind.

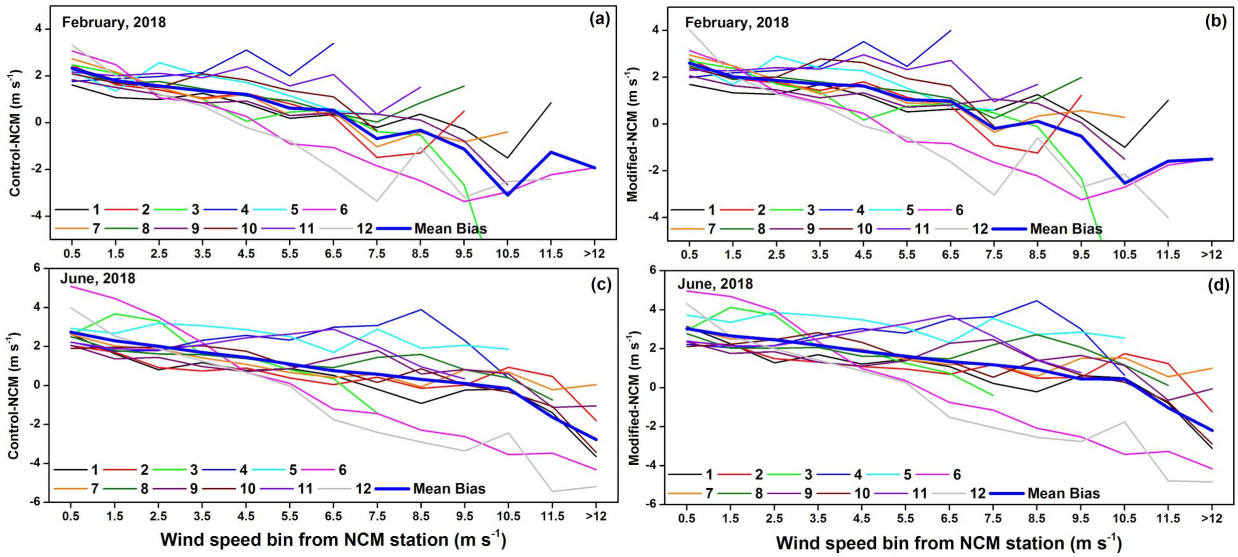

Figure 10. Bias in the 10-m wind speed (m s^{-1}) for different wind speed bins, for the simulations with the (a) control and (b) modified WRF configurations at the location of the 12 NCM weather stations (see *Figure 1(c)* for more details). (a-b) show the results for February 2018 and (c-d) for June 2018.

6. Discussion and Conclusions

The roughness length, a crucial parameter for land-atmosphere interactions [e.g. *Reijmer et al.*, 2004; *Jee et al.*, 2016; *June et al.*, 2018], is defined as the height above the surface at which the horizontal wind speed is zero, assuming that its variation in the surface layer follows a logarithmic profile [e.g. *Jiménez et al.*, 2012]. Empirically, z_{0m} is estimated as being about 1/10th of the height of the roughness elements [e.g. *Wallace and Hobbs*, 2006], but its representation in numerical models is challenging given the land surface heterogeneity within a model grid-box.

562 The common approach is to assign a value or range of values based on the dominant land-use
563 type [e.g. *Dong et al.*, 2018; *Campbell et al.*, 2019], which can be estimated from high temporal
564 frequency observations [e.g. *Reddy and Rao*, 2016] or remote sensing assets [e.g. *K Yang et al.*,
565 2008].

566 In this paper, the surface roughness length in a desert site in the UAE is estimated using
567 eddy-covariance measurements, and is found to be about one order of magnitude smaller than the
568 default value used in WRF, in the range 1.3 to 2.2 mm, as opposed to 10 mm. The estimated
569 $z_{0m}$is, however, within the range of values for barren regions, 0.2 – 2.74 mm [e.g. *Marticorena*
570 *et al.*, 2004; *Prigent*, 2005; *K Yang et al.*, 2008]. For a month in the winter (February 2018) and
571 summer (June 2018) seasons, the WRF model is run over the UAE with the default and
572 estimated roughness lengths, in a 12 km - 4 km - 1.333 km configuration, with the hourly
573 predictions of the latter two grids used for analysis. For both months, and in line with
574 expectations and previous studies [e.g. *Reijmer et al.*, 2004; *Wang et al.*, 2009], a reduced
575 roughness length leads to stronger near-surface winds by up to 1 m s^{-1}. As a result of a reduced
576 exchange coefficient for heat, the sensible heat flux is lower by up to 10 W m^{-2}. In order to keep
577 the surface energy budget closed, and given the lower values of H, the surface temperature
578 increases by up to 2.5ºC. The sign and magnitude of the changes in the surface temperature and
579 heat fluxes found here are also in line with those reported by other studies [e.g. *Giorgi*, 1997;
580 *Reijmer et al.*, 2004; *June et al.*, 2018].

581 In addition to a direct comparison of the two WRF products, the model predictions are
582 evaluated against weather station data provided by the NCM. At Al Ain, where the roughness
583 length estimation was conducted, WRF is found to over predict the observed 10-m wind speed
584 by roughly 0.5 m s^{-1}, in line with other studies in arid/semi-arid regions [e.g. *Gunwani and*

585 *Mohan*, 2017], slightly augmented in the modified configuration (maximum differences up to 1
586 m s^{-1}). However, the wind speed bias is dependent on the strength of the wind. In particular, it is
587 found that, while for low wind speeds < 4 m s^{-1} the two WRF configurations give comparable
588 predictions, for speeds mostly in excess of about 6 m s^{-1}, having a more realistic representation of
589 the observed roughness length generates more skillful forecasts, mostly by 1-3 m s^{-1}. A similar
590 dependence of the model wind speed predictions on the strength of the wind has been reported
591 by other authors [e.g. *Carvalho et al.*, 2012; *Q Yang et al.*, 2013], and may arise from an
592 incorrect representation of the turbulent mixing by the PBL scheme. When compared to the
593 predictions of the 4 km grid, the wind speeds predicted by the 1.333 km grid are generally more
594 accurate, with biases up to 3 m s^{-1} smaller compared to station data. For air temperature and H,
595 the simulation with the reduced roughness length is more skillful, being able to partially correct
596 the cold bias seen in the warm season which has been highlighted by *D Zheng et al.* [2013]. The
597 biases of these two fields are mostly in the range ±2ºC and ±100 W m^{-2}, respectively. The
598 conclusions reached at Al Ain also hold for other stations, in particular for those located in the
599 inland desert where the roughness length was modified.

600 The analysis conducted here highlighted potential deficiencies in the PBL scheme, in
601 particular with respect to the turbulent mixing and surface drag formulation. A further
602 improvement of the model forecasts can be obtained by optimizing tunable parameters used in
603 the PBL and surface layer schemes, as shown in *B Yang et al.* [2017]. Alternatively, a new
604 parameterization scheme tailored for arid/semi-arid regions can be developed and subsequently
605 implemented in the model. Some of these improvements will be presented in a subsequent paper.
606

Acknowledgments and Data

We acknowledge the National Center of Meteorology (NCM) for kindly providing weather station data used for model evaluation. This study is supported by the UAE Research Program for Rain Enhancement Science (UAEREP). Data used in the present analysis is available at https://kudrive.ku.ac.ae/oc-shib/index.php/s/sdUNPlvZlaP2JoC. We are also grateful to Hans-Dieter Wizemann from the University of Hohenheim for operating the eddy-covariance station and processing the raw measurements.

References

Alapaty, K., J. A. Herwehe, T. L. Otte, C. G. Nolte, O. R. Bullock, M. S. Mallard, J. S. Kain, and J. Dudhia (2012), Introducing subgrid-scale cloud feedbacks to radiation for regional meteorological and climate modeling, *Geophys Res. Lett.*, *39*(24), doi:10.1029/2012gl054031.

Borge, R., V. Alexandrov, J. José del Vas, J. Lumbreras, and E. Rodríguez (2008), A comprehensive sensitivity analysis of the WRF model for air quality applications over the Iberian Peninsula, *Atmos. Environ.*, *42*(37), 8560-8574, doi:https://doi.org/10.1016/j.atmosenv.2008.08.032.

Branch, O., and V. Wulfmeyer (2019), Deliberate enhancement of rainfall using desert plantations, *Proceedings of the National Academy of Sciences*, *116*(38), 18841, doi:10.1073/pnas.1904754116.

Businger, J. A., J. C. Wyngaard, Y. Izumi, and E. F. Bradley (1971), Flux-Profile Relationships in the Atmospheric Surface Layer, *J. Atmos. Sci.*, *28*(2), 181-189, doi:10.1175/1520-0469(1971)028<0181:FPRITA>2.0.CO;2.

Campbell, P. C., J. O. Bash, and T. L. Spero (2019), Updates to the Noah Land Surface Model in WRF-CMAQ to Improve Simulated Meteorology, Air Quality, and Deposition, *Journal of Advances in Modeling Earth Systems*, *11*(1), 231-256, doi:10.1029/2018MS001422.

Carvalho, D., A. Rocha, M. Gómez-Gesteira, and C. Santos (2012), A sensitivity study of the WRF model in wind simulation for an area of high wind energy, *Environ. Modell. Softw.*, *33*, 23-34, doi:10.1016/j.envsoft.2012.01.019.

Chaouch, N., M. Temimi, M. Weston, and H. Ghedira (2017), Sensitivity of the meteorological model WRF-ARW to planetary boundary layer schemes during fog conditions in a coastal arid region, *Atmos. Res.*, *187*, 106-127, doi:10.1016/j.atmosres.2016.12.009.

Charnock, H. (1955), Wind stress on a water surface, *Q. J. R. Meteorol. Soc.*, *81*(350), 639-640, doi:10.1002/qj.49708135027.

Chen, F., and J. Dudhia (2001), Coupling an Advanced Land Surface–Hydrology Model with the Penn State–NCAR MM5 Modeling System. Part I: Model Implementation and Sensitivity, *Mon. Weather Rev.*, *129*(4), 569-585, doi:10.1175/1520-0493(2001)129<0569:caalsh>2.0.co;2.

Cheng, W. Y. Y., and W. J. Steenburgh (2005), Evaluation of Surface Sensible Weather Forecasts by the WRF and the Eta Models over the Western United States, *Weather Forecast.*, *20*(5), 812-821, doi:10.1175/waf885.1.

Cullen, N. J., T. Mölg, G. Kaser, K. Steffen, and D. R. Hardy (2007), Energy-balance model validation on the top of Kilimanjaro, Tanzania, using eddy covariance data, *Annals of Glaciology*, *46*, 227-233, doi:10.3189/172756407782871224.

649 Dong, H., S. Cao, T. Takemi, and Y. Ge (2018), WRF simulation of surface wind in high latitudes,
650 *Journal of Wind Engineering and Industrial Aerodynamics*, *179*, 287-296,
651 doi:10.1016/j.jweia.2018.06.009.
652 Dudhia, J., and J. F. Bresch (2002), A Global Version of the PSU–NCAR Mesoscale Model, *Mon.*
653 *Weather Rev.*, *130*(12), 2989-3007, doi:10.1175/1520-0493(2002)130<2989:agvotp>2.0.co;2.
654 Dyer, A. J., and B. B. Hicks (1970), Flux-gradient relationships in the constant flux layer, *Q. J. R.*
655 *Meteorol. Soc.*, *96*(410), 715-721, doi:10.1002/qj.49709641012.
656 Eager, R. E., S. Raman, A. Wootten, D. L. Westphal, J. S. Reid, and A. Al Mandoos (2008), A
657 climatological study of the sea and land breezes in the Arabian Gulf region, *J. Geophys. Res.*, *113*(D15),
658 doi:10.1029/2007jd009710.
659 Giorgi, F. (1997), An Approach for the Representation of Surface Heterogeneity in Land Surface Models.
660 Part II: Validation and Sensitivity Experiments, *Mon. Weather Rev.*, *125*(8), 1900-1919,
661 doi:10.1175/1520-0493(1997)125<1900:aaftro>2.0.co;2.
662 Graf, A., A. van de Boer, A. Moene, and H. Vereecken (2014), Intercomparison of Methods for the
663 Simultaneous Estimation of Zero-Plane Displacement and Aerodynamic Roughness Length from Single-
664 Level Eddy-Covariance Data, *Boundary Layer Meteorol.*, *151*(2), 373-387, doi:10.1007/s10546-013-
665 9905-z.
666 Greeley, R., D. G. Blumberg, J. F. McHone, A. Dobrovolskis, J. D. Iversen, N. Lancaster, K. R.
667 Rasmussen, S. D. Wall, and B. R. White (1997), Applications of spaceborne radar laboratory data to the
668 study of aeolian processes, *Journal of Geophysical Research: Planets*, *102*(E5), 10971-10983,
669 doi:10.1029/97je00518.
670 Gunwani, P., and M. Mohan (2017), Sensitivity of WRF model estimates to various PBL
671 parameterizations in different climatic zones over India, *Atmos. Res.*, *194*, 43-65,
672 doi:10.1016/j.atmosres.2017.04.026.
673 Hari Prasad, K. B. R. R., C. Venkata Srinivas, C. Venkateswara Naidu, R. Baskaran, and B. Venkatraman
674 (2016), Assessment of surface layer parameterizations in ARW using micro-meteorological observations
675 from a tropical station, *Meteorol. Appli.*, *23*(2), 191-208, doi:10.1002/met.1545.
676 Högström, U. (1988), Non-dimensional wind and temperature profiles in the atmospheric surface layer: A
677 re-evaluation, *Boundary Layer Meteorol.*, *42*(1), 55-78, doi:10.1007/BF00119875.
678 Hong, S., V. Lakshmi, E. E. Small, F. Chen, M. Tewari, and K. W. Manning (2009), Effects of vegetation
679 and soil moisture on the simulated land surface processes from the coupled WRF/Noah model, *J.*
680 *Geophys. Res.*, *114*(D18), doi:10.1029/2008jd011249.

Iacono, M. J., J. S. Delamere, E. J. Mlawer, M. W. Shephard, S. A. Clough, and W. D. Collins (2008), Radiative forcing by long-lived greenhouse gases: Calculations with the AER radiative transfer models, *J. Geophys. Res.*, *113*(D13), doi:10.1029/2008jd009944.

Jee, J.-B., M. Jang, C. Yi, I.-S. Zo, B.-Y. Kim, M.-S. Park, and Y.-J. Choi (2016), Sensitivity Analysis of the High-Resolution WISE-WRF Model with the Use of Surface Roughness Length in Seoul Metropolitan Areas, *Atmosphere*, *26*(1), 111-126, doi:10.14191/atmos.2016.26.1.111.

Jesan, T., C. Manonmani, J. Brindha, S. Rajaram, P. M. Ravi, and R. M. Tripathi (2016), Estimation of roughness length Z0for Kalpakkam site, *Radiation Protection and Environment*, *39*(1), 44, doi:10.4103/0972-0464.185182.

Jiménez, P. A., J. Dudhia, J. F. González-Rouco, J. Navarro, J. P. Montávez, and E. García-Bustamante (2012), A Revised Scheme for the WRF Surface Layer Formulation, *Mon. Weather Rev.*, *140*(3), 898-918, doi:10.1175/mwr-d-11-00056.1.

June, T., A. Meijide, C. Stiegler, A. P. Kusuma, and A. Knohl (2018), The influence of surface roughness and turbulence on heat fluxes from an oil palm plantation in Jambi, Indonesia, *IOP Conf Ser Earth Environ Sci*, *149*, 012048, doi:10.1088/1755-1315/149/1/012048.

Kain, J. S. (2004), The Kain–Fritsch Convective Parameterization: An Update, *J. Appl. Meteorol.*, *43*(1), 170-181, doi:10.1175/1520-0450(2004)043<0170:tkcpau>2.0.co;2.

Kain, J. S., and J. M. Fritsch (1990), A One-Dimensional Entraining/Detraining Plume Model and Its Application in Convective Parameterization, *J. Atmos. Sci.*, *47*(23), 2784-2802, doi:10.1175/1520-0469(1990)047<2784:aodepm>2.0.co;2.

Kim, E.-J., and S.-Y. Hong (2010), Impact of air-sea interaction on East Asian summer monsoon climate in WRF, *J. Geophys. Res.*, *115*(D19), doi:10.1029/2009jd013253.

Komuscu, A. U. (2017), Long-term mean monthly temperatures trends of the United Arab Emirates, *International Journal of Global Warming*, *11*(1), 1, doi:10.1504/ijgw.2017.080987.

Li, D., E. Bou-Zeid, and H. A. R. De Bruin (2011), Monin–Obukhov Similarity Functions for the Structure Parameters of Temperature and Humidity, *Boundary Layer Meteorol.*, *145*(1), 45-67, doi:10.1007/s10546-011-9660-y.

Lu, L., S. Liu, Z. Xu, K. Yang, X. Cai, L. Jia, and J. Wang (2009), The characteristics and parameterization of aerodynamic roughness length over heterogeneous surfaces, *Advances in Atmospheric Sciences*, *26*(1), 180-190, doi:10.1007/s00376-009-0180-3.

Man Sing, W., Y. Jinxin, J. Nichol, W. Qihao, M. Menenti, and P. W. Chan (2015), Modeling of Anthropogenic Heat Flux Using HJ-1B Chinese Small Satellite Image: A Study of Heterogeneous Urbanized Areas in Hong Kong, *IEEE Geosci. Remote Sens. Lett.*, *12*(7), 1466-1470, doi:10.1109/lgrs.2015.2409111.

715 Marticorena, B., G. Bergametti, B. Aumont, Y. Callot, C. N'Doumé, and M. Legrand (1997), Modeling
716 the atmospheric dust cycle: 2. Simulation of Saharan dust sources, *J. Geophys. Res. Atmos.*, *102*(D4),
717 4387-4404, doi:10.1029/96jd02964.
718 Marticorena, B., P. Chazette, G. Bergametti, F. Dulac, and M. Legrand (2004), Mapping the aerodynamic
719 roughness length of desert surfaces from the POLDER/ADEOS bi-directional reflectance product, *Int. J.*
720 *Remote Sens.*, *25*(3), 603-626, doi:10.1080/0143116031000116976.
721 Massey, J. D., W. J. Steenburgh, S. W. Hoch, and J. C. Knievel (2014), Sensitivity of Near-Surface
722 Temperature Forecasts to Soil Properties over a Sparsely Vegetated Dryland Region, *J. Appl. Meteorol.*
723 *Climatol.*, *53*(8), 1976-1995, doi:10.1175/jamc-d-13-0362.1.
724 Meehl, G. A., and W. M. Washington (1988), A Comparison of Soil-Moisture Sensitivity in Two Global
725 Climate Models, *J. Atmos. Sci.*, *45*(9), 1476-1492, doi:10.1175/1520-
726 0469(1988)045<1476:acosms>2.0.co;2.
727 Menut, L., C. Pérez, K. Haustein, B. Bessagnet, C. Prigent, and S. Alfaro (2013), Impact of surface
728 roughness and soil texture on mineral dust emission fluxes modeling, *J. Geophys. Res. Atmos.*, *118*(12),
729 6505-6520, doi:10.1002/jgrd.50313.
730 Miller, M. J., A. C. M. Beljaars, and T. N. Palmer (1992), The Sensitivity of the ECMWF Model to the
731 Parameterization of Evaporation from the Tropical Oceans, *J. Clim.*, *5*(5), 418-434, doi:10.1175/1520-
732 0442(1992)005<0418:tsotem>2.0.co;2.
733 Mlawer, E. J., S. J. Taubman, P. D. Brown, M. J. Iacono, and S. A. Clough (1997), Radiative transfer for
734 inhomogeneous atmospheres: RRTM, a validated correlated-k model for the longwave, *J. Geophys. Res.*
735 *Atmos.*, *102*(D14), 16663-16682, doi:10.1029/97jd00237.
736 Naizghi, M. S., and T. B. M. J. Ouarda (2017), Teleconnections and analysis of long-term wind speed
737 variability in the UAE, *Int. J. Climatol.*, *37*(1), 230-248, doi:10.1002/joc.4700.
738 Nelli, N. R., M. Temimi, R. M. Fonseca, M. J. Weston, M. S. Thota, V. K. Valappil, O. Branch, H.-D.
739 Wizemann, V. Wulfmeyer, and Y. Wehbe (2020), Micrometeorological measurements in an arid
740 environment: Diurnal characteristics and surface energy balance closure, *Atmos. Res.*, *234*, 104745,
741 doi:10.1016/j.atmosres.2019.104745.
742 Paulson, C. A. (1970), The Mathematical Representation of Wind Speed and Temperature Profiles in the
743 Unstable Atmospheric Surface Layer, *J. Appl. Meteorol.*, *9*(6), 857-861, doi:10.1175/1520-
744 0450(1970)009<0857:TMROWS>2.0.CO;2.
745 Prigent, C. (2005), Estimation of the aerodynamic roughness length in arid and semi-arid regions over the
746 globe with the ERS scatterometer, *J. Geophys. Res.*, *110*(D9), doi:10.1029/2004jd005370.

747 Prueger, J. H., W. P. Kustas, L. E. Hipps, and J. L. Hatfield (2004), Aerodynamic parameters and sensible
748 heat flux estimates for a semi-arid ecosystem, *Journal of Arid Environments*, *57*(1), 87-100,
749 doi:10.1016/s0140-1963(03)00090-9.
750 Ran, L., J. Pleim, and R. Gilliam (2010), Impact of high resolution land-use data in meteorology and air
751 quality modeling systems, in *Air Pollution Modeling and its Application XX*, edited by D. G. Steyn and S.
752 T. Rao, p. 108, Springer Netherlands, Netherlands.
753 Rao, K. G. (1996), Roughness length and drag coefficient at two MONTBLEX-90 tower stations,
754 *Proceedings of the Indian Academy of Sciences - Earth and Planetary Sciences*, *105*(3), 273-287,
755 doi:10.1007/BF02841883.
756 Rao, K. G., G. Ramakrishna, and N. Narendra Reddy (2011), Impact of meso-net observations on short-
757 term prediction of intense weather systems during PRWONAM: Part I—On wind variations, *J. Atmos.*
758 *Sol. Terr. Phys.*, *73*(9), 965-985, doi:https://doi.org/10.1016/j.jastp.2010.08.019.
759 Reddy, N. N., and Kusuma G. Rao (2016), Roughness Lengths at Four Stations Within the
760 Micrometeorological Network over the Indian Monsoon Region, *Boundary Layer Meteorol.*, *158*(1), 151-
761 164, doi:10.1007/s10546-015-0080-2.
762 Reijmer, C. H., E. Van Meijgaard, and M. R. Van Den Broeke (2004), Numerical Studies with a Regional
763 Atmospheric Climate Model Based on Changes in the Roughness Length for Momentum and Heat Over
764 Antarctica, *Boundary Layer Meteorol.*, *111*(2), 313-337, doi:10.1023/b:boun.0000016470.23403.ca.
765 Shukla, J., and Y. Mintz (1982), Influence of Land-Surface Evapotranspiration on the Earth's Climate,
766 *Science*, *215*(4539), 1498-1501, doi:10.1126/science.215.4539.1498.
767 Skamarock, W. C., J. B. Klemp, J. Dudhia, D. O. Gill, D. M. Barker, and e. a. Duda (2008), A description
768 of the Advanced Research WRF version 3*Rep.*, 113 pp.
769 Stathopoulos, T. (2009), Wind and Comfort, in *5th European & African Conferences on Wind*
770 *Engineering (EACWE 5)*, edited, Florence, Italy.
771 Steeneveld, G. J., T. Mauritsen, E. I. F. de Bruijn, J. Vilà-Guerau de Arellano, G. Svensson, and A. A. M.
772 Holtslag (2008), Evaluation of Limited-Area Models for the Representation of the Diurnal Cycle and
773 Contrasting Nights in CASES-99, *J. Appl. Meteorol. Climatol.*, *47*(3), 869-887,
774 doi:10.1175/2007jamc1702.1.
775 Sud, Y. C., and W. E. Smith (1985), The influence of surface roughness of deserts on the July circulation,
776 *Boundary Layer Meteorol.*, *33*(1), 15-49, doi:10.1007/bf00137034.
777 Sukoriansky, S., B. Galperin, and V. Perov (2005), 'Application of a New Spectral Theory of Stably
778 Stratified Turbulence to the Atmospheric Boundary Layer over Sea Ice', *Boundary Layer Meteorol.*,
779 *117*(2), 231-257, doi:10.1007/s10546-004-6848-4.

780 Thompson, G., P. R. Field, R. M. Rasmussen, and W. D. Hall (2008), Explicit Forecasts of Winter
781 Precipitation Using an Improved Bulk Microphysics Scheme. Part II: Implementation of a New Snow
782 Parameterization, *Mon. Weather Rev.*, *136*(12), 5095-5115, doi:10.1175/2008mwr2387.1.
783 Valappil, V. K., M. Temimi, M. Weston, R. Fonseca, N. R. Nelli, M. Thota, and K. N. Kumar (2019),
784 Assessing Bias Correction Methods in Support of Operational Weather Forecast in Arid Environment,
785 *Asia-Pac. J. Atmos. Sci.*, doi:10.1007/s13143-019-00139-4.
786 Varquez, A. C. G., M. Nakayoshi, and M. Kanda (2015), The Effects of Highly Detailed Urban
787 Roughness Parameters on a Sea-Breeze Numerical Simulation, *Boundary Layer Meteorol.*, *154*(3), 449-
788 469, doi:10.1007/s10546-014-9985-4.
789 Wallace, J. M., and P. V. Hobbs (2006), *Atmospheric Science, Second Edition: An Introductory Survey*,
790 second ed., 504 pp., Academic Press.
791 Wang, X., Z. Wu, and G. Liang (2009), WRF/CHEM modeling of impacts of weather conditions
792 modified by urban expansion on secondary organic aerosol formation over Pearl River Delta,
793 *Particuology*, *7*(5), 384-391, doi:10.1016/j.partic.2009.04.007.
794 Weston, M., N. Chaouch, V. Valappil, M. Temimi, M. Ek, and W. Zheng (2018), Assessment of the
795 Sensitivity to the Thermal Roughness Length in Noah and Noah-MP Land Surface Model Using WRF in
796 an Arid Region, *Pure Appl. Geophy.*, *176*(5), 2121-2137, doi:10.1007/s00024-018-1901-2.
797 Yagoub, M. M. (2010), GIS for Wind Energy: A Case of UAE, *International Journal of Geoinformatics*,
798 *6*(3), 13-21.
799 Yang, B., Y. Qian, L. K. Berg, P.-L. Ma, S. Wharton, V. Bulaevskaya, H. Yan, Z. Hou, and W. J. Shaw
800 (2017), Sensitivity of Turbine-Height Wind Speeds to Parameters in Planetary Boundary-Layer and
801 Surface-Layer Schemes in the Weather Research and Forecasting Model, *Boundary Layer Meteorol.*,
802 *162*(1), 117-142, doi:10.1007/s10546-016-0185-2.
803 Yang, K., T. Koike, H. Ishikawa, J. Kim, X. Li, H. Liu, S. Liu, Y. Ma, and J. Wang (2008), Turbulent
804 Flux Transfer over Bare-Soil Surfaces: Characteristics and Parameterization, *J. Appl. Meteorol. Climatol.*,
805 *47*(1), 276-290, doi:10.1175/2007jamc1547.1.
806 Yang, Q., L. K. Berg, M. Pekour, J. D. Fast, R. K. Newsom, M. Stoelinga, and C. Finley (2013),
807 Evaluation of WRF-Predicted Near-Hub-Height Winds and Ramp Events over a Pacific Northwest Site
808 with Complex Terrain, *J. Appl. Meteorol. Climatol.*, *52*(8), 1753-1763, doi:10.1175/jamc-d-12-0267.1.
809 Zheng, D., R. van der Velde, Z. Su, M. J. Booij, A. Y. Hoekstra, and J. Wen (2013), Assessment of
810 Roughness Length Schemes Implemented within the Noah Land Surface Model for High-Altitude
811 Regions, *J. Hydrometeorol.*, *15*(3), 921-937, doi:10.1175/JHM-D-13-0102.1.

812 Zheng, W., H. Wei, Z. Wang, X. Zeng, J. Meng, M. Ek, K. Mitchell, and J. Derber (2012), Improvement
813 of daytime land surface skin temperature over arid regions in the NCEP GFS model and its impact on
814 satellite data assimilation, *J. Geophys. Res. Atmos.*, *117*(D6), D06117, doi:10.1029/2011jd015901.
815 Zhu, M., and B. W. Atkinson (2004), Observed and modelled climatology of the land–sea breeze
816 circulation over the Persian Gulf, *Int. J. Climatol.*, *24*(7), 883-905, doi:10.1002/joc.1045.

817